ROYAL SOCIETY
OF CHEMISTRY

www.rsc.org/materialsA
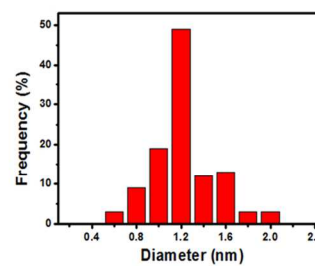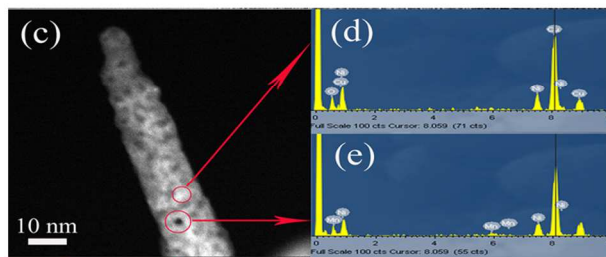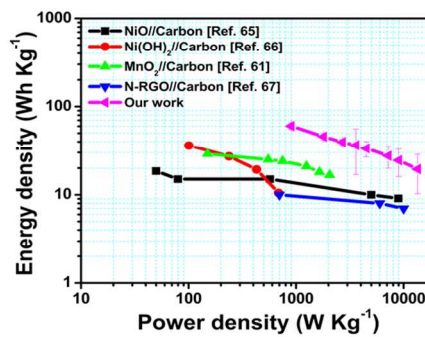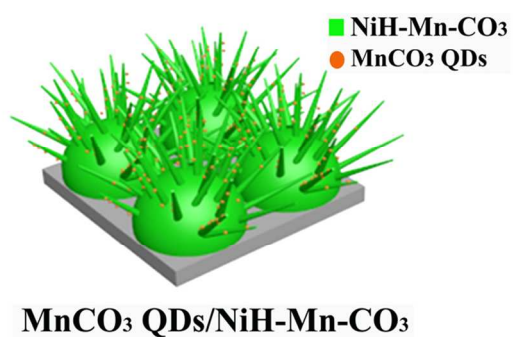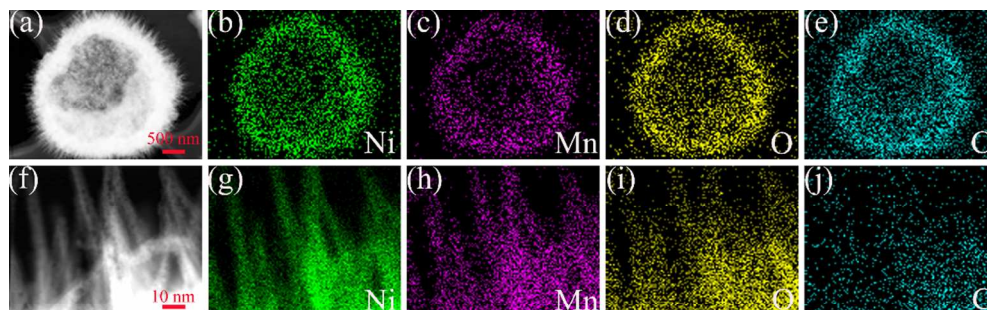
337x330mm (96 x 96 DPI)

Facile Synthesis of Manganese Carbonate Quantum Dot/Ni(HCO$_3$)$_2$-MnCO$_3$ Composites as Advanced Cathode Materials for High Energy Density Asymmetric Supercapacitors

Qi Xun Xia[a], Kwan San Hui[b], Kwun Nam Hui[a,] Sung Dae Kim[c], Jae Hong Lim[d], Si Young Choi[c], Luo Jiang Zhang[b], Rajaram S. Mane[e], Je Moon Yun[f] and Kwang Ho Kim[f,a*]*

[a]School of Materials Science and Engineering, Pusan National University San 30 Jangjeon-dong, Geumjeong-gu, Busan 609-735, Republic of Korea
[b]Department of Mechanical Convergence Engineering, Hanyang University 17 Haengdang-dong, Seongdong-gu, Seoul 133-791, Republic of Korea
[c]Advanced Characterization and Analysis Group, Korea Institute of Materials Science (KIMS), Changwon 642-831, Republic of Korea
[d]Materials Processing Division, Korea Institute of Materials Science (KIMS), Changwon 642-831, Republic of Korea
[e]School of Physical Sciences, Swami Ramanand Teerth Marathwada University Nanded 431606, India
[f]Global Frontier R&D Center for Hybrid Interface Materials, Pusan National University, 30 Jangjeon-dong, Geumjung-gu, Busan 609-735, South Korea

E-mail: bizhui@pusan.ac.kr; kwhokim@pusan.ac.kr

Keywords: core-shell structure; nickel foam; graphene; binder-free; asymmetric supercapacitors

Abstract

We have developed a high performance supercapacitor cathode electrode composed of well dispersed MnCO$_3$ quantum dots (QDs, ~ 1.2 nm) decorated on nickel hydrogen carbonate-manganese carbonate (Ni(HCO$_3$)$_2$-MnCO$_3$) hedgehog-like shell@needle (MnCO$_3$ QDs/NiH-Mn-CO$_3$) composites directly onto a 3D macro-porous nickel foam as a binder-free supercapacitor electrode by a facile and scalable hydrothermal method. Due to different growths of Ni(HCO$_3$)$_2$ and MnCO$_3$, MnCO$_3$

segregation gave rise to the formation of $MnCO_3$ QDs on the NiH-Mn-CO_3 nanoneedles surface. The $MnCO_3$ QDs/NiH-Mn-CO_3 composites electrode exhibited a remarkable maximum specific capacitance of 2641.3 F g^{-1} at 3 A g^{-1} and 1493.3 F g^{-1} at 15 A g^{-1}. Moreover, the asymmetric supercapacitor with $MnCO_3$ QDs/NiH-Mn-CO_3 composites as the positive electrode and graphene as the negative electrode, showed an energy density of 58.1 Wh kg^{-1} at a power density of 900 W kg^{-1} as well as excellent cycling stability with 91.3% retention after 10000 cycles, which exceeded the energy densities of most previously reported nickel or manganese oxide/hydroxide-based asymmetric supercapacitors. The ultrahigh capacitive performance is attributed to the presence of high surface area core-shell nanostructure, the well dispersed $MnCO_3$ quantum dots, high conductivity of $MnCO_3$ quantum dots as well as the synergetic effect between multiple transition metal ions. The superior supercapacitive performance of the $MnCO_3$ QDs/NiH-Mn-CO_3 composites makes it become a promising cathode materials for high energy density asymmetric supercapacitors.

Introduction

With the sharp increase in the world energy-use over the past few decades, there has been considerable interest in searching for high-performance energy storage systems, such as lithium ion batteries[1] and supercapacitors (SCs). SCs have attracted

considerable interest over the past few decades owing to their fast charge and discharge rates, high power density, long cycle life, and higher reliability than that of lithium ion batteries.[2-4] Generally, SCs can be divided into two types, which rely on different electron storage mechanisms: electrical double layer capacitors (by ion adsorption) and pseudocapacitors (by rapid surface redox reactions). Pseudocapacitors normally utilize transition metal oxides/hydroxides as electrode materials,[5, 6] producing capacitances exceeding those of double-layer carbonaceous materials. Therefore, the pseudocapacitive performance has been studied extensively.[7, 8]

Among metal oxide materials, nickel or manganese based oxides are used widely to prepare electrodes for supercapacitors because of their high theoretical specific capacitance (2583 F g^{-1} for NiO and 1370 F g^{-1} for MnO_2),[9, 10] the relatively low cost, high redox activity, and environmentally friendly nature.[11-13] In particular, binary Ni-Mn compounds, such as oxides, hydroxides, and sulfides,[14-16] have been reported to exhibit superior electrochemical performance to that of single metal components owing to their richer redox reactions from both nickel and manganese ions. Thus far, a large variety of binary nickel-manganese compounds with different morphologies, such as nanoparticles,[17] nanoneedles,[16] nanosheets,[18] nanowires,[19] and porous plates[20] have been reported. H. Jiang et al. reported a $Ni(OH)_2$ nanowire-MnO_2 nanoflake core-shell nanostructure electrode material, showing a specific capacitance of 355 F g^-

[1] (at 0.5 A/g).[21] Rusi et al. reported a MnO_2/NiO binary metal oxide film as an electrode materials, exhibiting a specific capacitance of 681 F g^{-1} (at 1 A/g).[22] H. Wan et al. synthesized hedgehog-like hollow Ni-Mn oxides for supercapacitor electrodes that showed a high capacitance of 1016 F g^{-1} (at 0.5 A/g).[16] Recently, J.Sun et al. fabricated a 3D core/shell structure composed of MnOOH/NiO nansheets for supercapacitors with a very high specific capacitance of 1890.5 F g^{-1} (at 1.7 A g^{-1}).[23] On the other hand, there are few reports on the electrochemical performance of binary nickel hydrogen carbonate-manganese carbonate hedgehog-like shell@needle composites. To achieve an optimized overall electrochemical performance, rationally designed electrode structures with proper selection of core-shell architechture and well dispersion of small size particles, in particular, quantum dots, are highly desirable for achiving high specific capacitance and good rate capacibility owing to a superior high surface area, high conductivity of nanoparticles, inhibition of aggregations, and shorten diffusion length for electrolye ions.[24-26] In this paper we present for the first time a facile and scalable hydrothermal method of growing 3D hierarchical $Ni(HCO_3)_2$-$MnCO_3$ hedgehog-like shell@needle core-shell (NiH-Mn-CO_3) composite on Ni foam, in which manganese carbonate hydroxide quantum dots ($MnCO_3$ QDs) with a mean diameter of ~1.2 nm were self-assembled due to different growths of $Ni(HCO_3)_2$ and $MnCO_3$, $MnCO_3$ segregation gave rise to the formation of $MnCO_3$ QDs on the NiH-Mn-CO_3 nanoneedles surface.[27] The as-obtained $MnCO_3$ QDs/NiH-Mn-CO_3 composites played an important roles in achieving high specific

4

capacitance. Specifically, (1) the hedgehog-like nanoneedle offers a large specific surface area that greatly improves the electrode/electrolyte contact area and shortens the ion diffusion paths; (2) shell@needle core-shell structure provides large opened channels in the nanoneedles for enhancing ion and electron diffusion, facilitating easier electrolyte penetration, and utilizing the active materials; (3) the interconnected nanostructure consisting of nanoshell@nanoneedles helps alleviate the structural damage caused by volume expansion during cycling, resulting in enhanced stability; (4) the small diameter of the nanoneedles and quantum dots lead to a high surface area, high conductivity of nanoparticles that contributes to the high capacitance; and (5) the single-crystalline nature of nanoneedles and quantum dots increases the electron transfer kinetics, contributing to improved cycling stability during cycling. The as-obtained $NiH-Mn-CO_3$ composites are different from the previously reported core-shell nanostructures.[14, 16, 18] Herein, the $MnCO_3$ QDs were anchored uniformly to the surface of the $NiH-Mn-CO_3$ composites, which offers additional advantages of superior pseudocapacitance due to the synergistic effects of binary metal compounds. In addition, an asymmetric supercapacitor with $MnCO_3$ QDs/$NiH-Mn-CO_3$ composites as positive and graphene (G) as negative electrode ($MnCO_3$ QDs/$NiH-Mn-CO_3$//G) exhibited a reversibly cycle at a high potential of 1.8 V and showed an energy density of 58.1 Wh kg^{-1} at a power density of 900 W kg^{-1}. An energy density of 17.9 Wh kg^{-1} at a high power density of 13.5 kW kg^{-1} was obtained at a high discharge current of 5 A g^{-1}, which exceeded the energy densities of most previously

reported nickel or manganese oxide/hydroxide-based asymmetric supercapacitors (Supporting Information Table S2). The as-obtained asymmetric supercapacitor exhibited excellent cycling stability, whereby a specific capacitance of 91.3% was retained after 10000 cycles.

Experimental section

Materials: Concentrated hydrochloric acid (37%, HCl) was obtained from Daejung Chemicals (Korea). Nickel nitrate hexahydrate (>97%, $Ni(NO_3)_2 \cdot 6H_2O$), manganese nitrate tetrahydrate ($Mn(NO_3)_2 \cdot 4H_2O$), urea ($(NH_2)_2CO$), and potassium hydroxide (KOH) were purchased from Sigma Aldrich. Acetone and anhydrous ethanol were supplied by SK Chemical (Korea).

Preparation of $MnCO_3$ QDs/$Ni(HCO_3)_2$-$MnCO_3$ composites: Pretreatment of a Ni foam, measuring1 cm x 1 cm with a pore density of 110 PPI and a mass density of 320 g/m^2 (Artenano Company Limited, Hong Kong) consisted of the following steps: degreasing by immersion in acetone for 30 min; etching with dilute HCl (3.0 mol/L) for 15 min, and rinsing with deionized water and drying. After pretreatment of the Ni foam, the precursors for the growth of $MnCO_3$ QDs/$Ni(HCO_3)_2$-$MnCO_3$ composite s were prepared. 6 mmol $Ni(NO_3)_2$ $\cdot 6H_2O$, 2 mmol $Mn(NO_3)_2 \cdot 4H_2O$, and 26.5 mmol urea were dissolved in 50 mL of deionized (DI) water and mixed homogeneously under ultrasonication for 30 min at room temperature. The cleaned nickel foam was then placed into a 50 mL Teflon autoclave with a homogeneous solution of precursor

and kept at 160 °C for 12 h. The nickel foam substrate covered with $MnCO_3$ QDs/NiH-Mn-CO_3 composites was washed with DI water ethanol to remove the surface ions and molecules, followed by vacuum-drying under 50 °C for 12 h. The mass of the active materials on Ni foam was determined by subtracting the weight before deposition from the weight after deposition. The loading densities of the active materials were approximately 2 mg cm^{-2} for all electrodes. For comparison, the $Ni(HCO_3)_2$ nanosheet sample was also prepared under the same conditions without adding Mn precursor.

Preparation of graphene-nickel foam electrodes: Graphite oxide (GO) was prepared from graphite powder using a modified Hummers method.[28-30] In a typical reaction, H_2SO_4 (180 mL) was added into the 2000 mL flask filled with graphite (8 g) and $NaNO_3$ (4 g) at room temperature, followed by the addition of solid $KMnO_4$ (23 g) slowly at 0 °C (ice bath). After increasing the temperature to 35 °C, the mixture was stirred vigorously for 180 min. Next, 375 mL of distilled water was added gradually at 0 °C, and the solution was stirred for 5 h while the temperature was increased to 90 °C. Finally, the solution was diluted with 1000 mL of distilled water and treated with H_2O_2 (30 wt.%) until no gas was produced, turning the color from dark brown to yellow. The solution was then filtered through a glass filter, washed with a 5% HCl solution and then washed again with distilled water. The GO suspension was freeze-dried at -70 °C for 7-8 h obtain the GO. A thermal expansion process was performed

at 1050 °C for 30 s in an Ar atmosphere to obtain the 3D porous GO. 3D porous

graphene was obtained from 3D porous GO by a reduction process at 450 °C for 2.5 h

in an Ar:H_2=2:1 forming gas atmosphere. The working electrodes were constructed

by mixing the active material, acetylene black and poly (tetrafluoroethylene) (PTFE)

suspension (60 wt.%) binder at a weight ratio of 8:1:1, and then pressed onto a nickel

foam (20 MPa), which served as a current collector. The electrodes were dried in a

vacuum oven at 60 °C for 12 h.

Material Characterization: The phase was characterized by X-ray diffraction (XRD,

D8-Discovery Brucker, Cu Kα, 40 kV, 40 mA). Scanning electron microscopy (SEM,

Hitachi, S-4800, 15 kV) equipped with an energy dispersive X-ray spectrometer

(EDX) was used to examined the morphology of the samples. The structure of the

porous hollow shell was investigated by transmission electron microscopy (TEM,

JEOL, JEM-2010F). The Brunauer-Emmett-Teller (BET) surface area was obtained

using a Micromeritics ASAP 2010 analyzer. The N_2 adsorption-desorption isotherm

and pore size distribution of the $Ni(HCO_3)_2$ and the $MnCO_3$ QDs/NiH-Mn-CO_3

composite samples were obtained by sonication from the Ni foam. X-ray

photoelectron spectroscopy (XPS, VG Scientifics ESCALAB250) was performed to

analyze the chemical bonding status of the $MnCO_3$ QDs/NiH-Mn-CO_3 composite.

The XPS spectra of the $MnCO_3$ QDs/NiH-Mn-CO3 composite powder were obtained

after sonication from the Ni foam, and were calibrated to the carbon peak C 1s at

284.6 eV.

Electrochemical Performance Measurements: The electrochemical measurements were carried out in a three electrode electrochemical cell containing a 1 M KOH aqueous solution as the electrolyte at room temperature. A Pt plate (facing to the working electrode) and Hg/Hg_2Cl_2 were used as the counter and reference electrode, respectively. The distance between the working and counter electrodes was approximately 1 cm. Cyclic voltammetry (CV) measurements and galvanostatic charge/discharge tests were performed on an Ivium-n-Stat electrochemical workstation (Ivium, Netherlands). For each type of the electrodes ($Ni(HCO_3)_2$ and $MnCO_3$ QDs/NiH-Mn-CO_3), the average values of the three sets of independent experiments (deviations within $\pm$ 5%) were reported using three different batches of the samples.

Calculations: The specific capacitance (C) of the electrode was calculated using the following equation:[9]

$$C_{\text{electrode}} = \frac{I\, \Delta t}{m\, \Delta V} \tag{1}$$

where C (F/g) is the specific capacitance, I (mA) is the discharge current, and m (mg), Δ V (V) and Δ t (s) are the designated mass of the active materials, potential drop during discharge and discharge time, respectively. The gravimetric specific capacitance was calculated by dividing capacitance by the mass of the electrode

material.

The C_{device} of asymmetric supercapacitor was calculated from the galvanostatic charge-discharge curves as follows:[31, 32]

$$C_{device} = \frac{I \, \Delta t}{M \, \Delta V} \tag{2}$$

where I (A) is the discharge current, Δt (s) is the discharge time, M (g) is the total mass of the active material in the positive and negative electrodes, and ΔV (V) is the voltage change (excluding the IR drop) within the discharge time.

The energy density (Wh Kg^{-1}) and power density (W Kg^{-1}) of the MnCO$_3$ QDs/NiH-Mn-CO$_3$ composites film, graphene electrodes, and asymmetric supercapacitor derived from the charge/discharge curves were calculated using the following equations;[9, 33]

$$E = 0.5 \times C_{device} \times \Delta V^2 / 3.6 \tag{3}$$

$$P = E/\Delta t \tag{4}$$

where E (Wh kg^{-1}) is the energy density, ΔV (V) is the device voltage excluding the IR drop, P (W kg^{-1}) is the average power density, and Δt (s) is the discharge time.

Results and discussion

The growth of Ni(HCO$_3$) nanosheets and MnCO$_3$ QDs/NiH-Mn-CO$_3$ composites on macro-porous nickel foam under hydrothermal conditions can be explained as follows. The growth of the Ni(HCO$_3$) nanosheets depends on the urea concentration and the extent of urea decomposition. First, CO$_3^{2-}$ and NH$_4^+$ are released via urea

decomposition; HCO_3^- and OH^- are generated through their hydration. A previous study reported that at low urea concentrations (< 4 mmol), the generation of OH^- is predominant and $Ni(OH)_2$ precipitates.[34] In the 5-10 mmol concentration range of urea, HCO_3^- and OH^- are present, and $Ni(OH)_2$ and $Ni(HCO_3)_2$ coexist. When urea concentration exceeds 20 mmol, the generation of HCO_3^- is dominant during ureolysis; thus, $Ni(HCO_3)_2$ is formed. In this study, 26.5 mmol urea was used to grow the $Ni(HCO_3)_2$ nanosheet architecture and the pH before hydrothermal growth was 5.58. Upon addition of the Mn^{2+} precursor source from $Mn(NO_3)_2 \cdot 4H_2O$, the pH decreased to 3.12 before hydrothermal growth. The formation mechanism of the as-obtained $Ni(HCO_3)_2$-$MnCO_3$ hedgehog-like shell@needle composites is similar to that reported in a nickel-manganese compounds study.[16] The formation mechanism is illustrated as follows: 1) Ni^{2+} reacts with HCO_3^- from ureolysis to form a nucleation center; 2) the nucleation center absorbs Mn^{2+} and forms flocculent nanostructures on the surface of the nuclei; and 3) as the Mn^{2+} induction process continues, the interior of the nuclei gradually form hollow structures, resulting in a hollow hedgehog-like structure.[16] The as-obtained $MnCO_3$ QDs/NiH-Mn-CO_3 core-shell composites work as a positive electrode, and an aqueous asymmetric supercapacitor was assembled, where the negative electrode was made from graphene, as illustrated in Scheme 1.

11

Fig. 1a shows the field-emission scanning electron microscopy (FESEM) images of the as-obtained porous $Ni(HCO_3)_2$ nanosheet arrays grown uniformly on the 3D macro-porous Ni foam, indicating clearly that the as-obtained $Ni(HCO_3)_2$ nanosheet arrays are comprised of many wrinkled nanosheets and are self-assembled perpendicular to the surface of the Ni foam. The resulting nanosheet arrays have a high porosity and an open structured with an average nanosheet thickness of less than 20 nm, and the gaps between the nanosheets varied from 30 nm to 80 nm (Fig. 1b). The high magnification TEM image shows the ultrathin nanosheet nanostructure (Fig. 1c). The hierarchical $MnCO_3$ QDs/NiH-Mn-CO_3 composites had a mean diameter of 2 μm and was composed of numerous 1D needle-like arrays, as shown in Fig. 1d-e. High magnification TEM revealed a needle, approximately 300 nm in length and 20 nm in diameter. The dark contrast inside the shell showed that the hybrid hedgehog-like composite consisted of a hollow shell structure, as shown in Fig. 1S (Supporting Information). This unique feature could provide a high active surface area, improve the electrode/electrolyte contact area, and shorten the ion diffusion paths, which could contribute to the enhanced electrochemical performance. Interestingly, a new type of NiH-Mn-CO_3 structure with jackfruit-like morphology was found near the node position of the Ni foam, as shown in Fig. 2S (Supporting Information). The high magnification SEM image (Fig. S2, Supporting Information) showed that jackfruit-like balls, approximately 120.5 μm in diameter, with a regular tetrahedron of the width of 1.5 μm grown vertically on Ni foam,

12

forming many columnar arrays. Fig. S3 presents the results of energy dispersive X-ray spectroscopy (EDS) mapping analysis of the image shown in Fig. S2 (Supporting information). The results confirm both Ni and Mn homogeneous distribution in the jackfruit-like ball structure. The mapping result is consistent with EDS (Fig. S2, Supporting information). To illustrate the chemical components and their spatial distribution in the Ni-Mn-CO_3 structure, EDS mapping was examined. Fig. 2 shows the TEM images and EDS-mapping images of the Ni, Mn, O, and C elements taken from the hedgehog-like Ni-Mn-CO_3 whole structure (Fig. 2a-e) and its nanoneedle regions (Fig. 2f-j). Results clearly confirm the well-defined hedgehog-like NiH-Mn-CO_3 structure with Ni, Mn, O, and C atoms unifromly distrubuted within the whole hollow core and nanoneedle shell structures, demonstrating that the sample is composite. More importantly, the distribution of Mn is found only to be on the surface of nanoneedles (Fig. 2h), confirming the present of $MnCO_3$ quantum dots on the surface of nanoneedles.

Fig. 3a shows the typical X-ray diffraction (XRD) patterns of the $Ni(HCO_3)_2$ and $MnCO_3$ QDs/NiH-Mn-CO_3 composite. The well-defined diffraction peaks observed at 14.9^o, 26.0^o, 33.7^o, 37.1^o, 40.1^o, 43.1^o, 45.9^o, 48.5^o, 55.8^o, and 62.6^o 2θ were indexed to (110), (211), (310), (222), (321), (400), (330), (420), (510), and (440) planes, respectively, for a $Ni(HCO_3)_2$ phase (JCPDS 15-0782). New peaks at 24.3^o, 31.6^o, 34.4^o, 41.7^o, 52.2^o, 60.4^o and 66.8^o 2θ were assigned to (012), (104), (006),

(113), (116), (122) and (125) of the MnCO$_3$ phase (JCPDS 01-86-0172), showing

that the hedgehog-like shell@needle structure is a composite consisting of two

phases.

High-resolution XPS was used to characterize the valence states of the elements of the

obtained hybrid shell-needle material, as shown in Fig. 3b-d. Two obvious shakeup

satellites (indicated as "Sat") and the Ni 2p$_{3/2}$ and Ni 2p$_{1/2}$ peaks were observed at

856.8 and 874.7 eV, indicating the presence of Ni^{2+} (Fig. 3b).[35] The Mn 2p peak

deconvolution shows three peaks attributing to Mn^{2+} (640.6 eV), Mn^{3+} (642.0 eV) and

Mn^{4+} (644.4 eV), respectively (Fig. 3c).[36] In the carbon 1s spectrum (Fig. 3d), the

binding energy peaks at 284.5 eV, 285.9 eV and 289.7 eV were assigned to the

characteristic bands of C-Mn C-O and C-OO, respectively, indicating the presence of

carbonate.[37] The O 1s spectra (Fig. S4, Supporting Information) shows the main peak

at 532.2 eV ascribing to surface-adsorbed oxygen from the oxide defects.[38] These

results clearly show that the abundance of oxygen defects and plenty of electroactive

sites, such as, Ni^{2+} and Mn^{4+}/Mn^{3+}/Mn^{2+} in the MnCO$_3$ QDs/NiH-Mn-CO$_3$ composites,

which is beneficial to high rate capacity the and long-term cycling stability of

pseudocapacitors.

The structural characteristics of the samples were further investigated by TEM.

Low-magnification TEM of Ni(HCO$_3$)$_2$ nanosheet indicated a hierarchical porous

nanosheet structured composed of ultrathin nanosheets, 10-20 nm in thickness, as shown in Fig. 4a, which agrees well with the morphology shown in Fig. 1b. The high-resolution TEM (HRTEM) image (Fig. 4b) revealed three different kinds of lattice fringes with spacings of 0.198, 0.222 and 0.208 nm corresponding to the (330), (321) and (400) planes of $Ni(HCO_3)_2$, respectively. Fig. 4c shows the fast Fourier transformation (FFT) pattern of the HRTEM image of the $Ni(HCO_3)_2$ nanosheet, indicating that the nanosheets are polycrystalline. Fig. 4d-f provide structural information on the $MnCO_3$ QDs/NiH-Mn-CO_3 composites. The low-magnification TEM image showed that a single nanoneedle was 16.1 nm in diameter (Fig. 4d). This hedgehog-like nanoneedle ball had a larger surface area than the $Ni(HCO_3)_2$ nanosheets, which was confirmed by BET-BJH analysis. HRTEM (Fig. 4e) revealed five different kinds of lattice fringes with spacings of 0.224, 0.244 and 0.263 nm, corresponding to the (321), (222) and (310) planes of $Ni(HCO_3)_2$, and spacings of 0.214 and 0.239 nm, corresponding to the (113) and (110) of $MnCO_3$, respectively. Fig. 4f displays the FFT pattern of the corresponding HRTEM image of the $MnCO_3$ QDs/NiH-Mn-CO_3 nanoneedle (Fig. 4e), indicating that the nanoneedles are polycrystalline.

Additional HRTEM measurements were performed on the nanoneedles of the $MnCO_3$ QDs/NiH-Mn-CO_3 composites. Fig. 5a shows that the surface of the nanoneedle is rough and irregular, which is different from the smooth and neat shape

15

of the nanoneedle, suggesting that $MnCO_3$ quantum dots are anchored to the

nanoneedle surface. The observed fringes with spacing 0.238 nm were assigned to

the (110) plane of $MnCO_3$ (Fig. 4b). Fig. 4c presents an annular dark-field (ADF)

scanning transmission electron microscopy (STEM) image of the polarized

nanoneedle of the $MnCO_3$ QDs/NiH-Mn-CO_3 composites. The bright area represents

Ni, whereas the dark area represents Mn. The corresponding EDS spectrum in Fig.

5c confirmed the distribution of both Mn and Ni throughout the needle structure (Fig.

5d and 5e). Fig. 5f-g showed the size distribution of $MnCO_3$ QDs with a mean

diameter of 1.2 nm.

To further check the possibility of interconnected pores in the materials and to

determine the surface area of the samples, N_2 adsorption/desorption isotherms and

the BJH pore size distribution plots of the porous structure of $Ni(HCO_3)_2$ and

$MnCO_3$ QDs/NiH-Mn-CO_3 composite samples were obtained, as shown in Fig. 6,

respectively, and Table 1 lists the specific textural properties. The isotherm of

$Ni(HCO_3)_2$ (red solid square line in Fig. 6) can be classified as a H3 type hysteresis

loop, which exhibits the presence of a typical macroporous structure of different

sizes according to the IUPAC classification. Based on the pore size distribution plot,

two well distinguished maxima centered at *ca.* 1.1 and *ca.* 12.5 nm can be observed,

corresponding to the results of the isotherm. The surface and interparticle spacing as

well as the internal voids contribute to the characteristic pore size distribution of a

material.[37] Therefore, the ripple-shaped porous network and the random attachment

of curly $Ni(HCO_3)_2$ nanosheets are the apparent reason for the pore size distribution

of the $Ni(HCO_3)_2$ nanosheet arrays. For the $MnCO_3$ QDs/NiH-Mn-CO_3 composite

(green solid triangle line of Fig. 6), a type-III isotherm with a H3 type hysteresis

loop and the pore size distribution centered at *ca.* 1.1 nm can be observed, indicating

a typical macroporous structure. The mean pore size, BET specific surface area and

the corresponding pore volume of $Ni(HCO_3)_2$ and $MnCO_3$ QDs/NiH-Mn-CO_3

composite, respectively, are 10.6 and 2.4 nm, 33.0 and 117.8 m^2 g^{-1}, and 0.19 and

0.45 cm^3 g^{-1}, respectively. The BET specific surface area and pore volume of the

$MnCO_3$ QDs/NiH-Mn-CO_3 composite were much higher than that of the $Ni(HCO_3)_2$

nanosheets sample and the reported nanoneedle nanomaterials, such as TiO_2,[39]

$NiCo_2O_4$.[40, 41] Such a distinct porous structure offers efficient transport pathways to

their interior voids during the charge/discharge storage process, which is essential

for the electrochemical performance, particularly for high-rate applications.

Electrochemical evaluation

The electrochemical properties of the $Ni(HCO_3)_2$ nanosheet and $MnCO_3$ QDs/NiH-

Mn-CO_3 composite structure as electrode materials for supercapacitors were

evaluated by cyclic voltammetry (CV), electrochemical impedance spectroscopy

(EIS), galvanic charge-discharge and cyclic stability in a three-electrode cell with a

Hg/Hg$_2$Cl$_2$ reference electrode and 1 M KOH aqueous electrolyte. Fig. 7a shows the

CV curves of the Ni(HCO$_3$)$_2$, MnCO$_3$ QDs/NiH-Mn-CO$_3$ composite and nickel

foam electrodes at a scan rate of 10 mV s^{-1} from which a pair of redox peaks with an

anodic peak at ~0.51 V and a cathodic peak at ~0.09 V was observed for Ni(HCO$_3$)$_2$

electrode, compared to a pair of redox peaks with an anodic peak at ~0.47 V and a

cathodic peak at ~0.1 V of a Ni-Mn-CO$_3$ composite electrode. In the case of nickel

foam, a flat line was deriving from nickel foam in CV curve, indicating that the

electrochemical performance of nickel foam is negligible.[42-44] This indicated the

strong pseudocapacitive nature of both electrodes. The peaks correspond to

conversion between the different oxidation states of Ni according to Equations 5 - 6:

$$3MnCO_3 + 3H_2O \rightleftarrows 3Mn^{2+} + 3HCO_3^- + 3OH^- \tag{5}$$

$$Ni(HCO_3)_2 + 3OH^- \rightleftarrows NiOOH + 2HCO_3^- + H_2O + e^-$$

(6)

In general, the smaller the potential difference between the anodic and

cathodic peak potential (ΔE), the better the reversibility in the redox reaction.

As shown in Fig. 7a, the MnCO$_3$ QDs/NiH-Mn-CO$_3$ composite electrode

(ΔE=370 mV) showed better reversibility than the Ni(HCO$_3$)$_2$ electrode

(ΔE=420 mV). This was attributed to the larger surface area of the Ni-Mn-

CO$_3$ composite electrode exposed to the electrolyte, which promoted the

efficient diffusion of OH$^-$ ions during the redox reactions.[45] Fig. 7b-c presents

the CV curves of the Ni(HCO$_3$)$_2$ and MnCO$_3$ QDs/NiH-Mn-CO$_3$ composite

electrodes, respectively, at different scan rates of 5, 10, 20, 30, 40, and 50 mV

s^{-1}. After increasing the scan rate, the anodic and cathodic peaks of both

electrodes in the CV curves shifted towards a positive and negative potential,

respectively, leading to a continuous increase in the potential distance

between the oxidation and reduction peaks. This indicates the quasi-reversible

feature of the redox couples. This observation was attributed to the Ohmic

resistance and increasing polarization of the electrode when the electrolyte

ions diffused in the porous electrode during the redox reaction at high scan

rates.[46] In Fig. 7a, compared to the Ni(HCO$_3$)$_2$ electrode, the CV curve of the

MnCO$_3$ QDs/NiH-Mn-CO$_3$ composite electrode showed higher peak currents

and larger integrated areas, indicating a higher specific capacitance. The

results suggest that the shell-needle architecture has a positive effect on the

capacitive performance of the electrode due to the high specific surface area.

This contributes to the high capacitance, which agrees well with the BET

specific surface area shown in Fig. 6. Fig. 7d shows the relationships between

the cathodic peak current ($I_{p,c}$) and the scan rate (v) of the Ni(HCO$_3$)$_2$ and

MnCO$_3$ QDs/NiH-Mn-CO$_3$ composite ectrodes. $I_{p,c}$ increased linearly with

$v^{1/2}$, confirming that the pseudocapacitive nature of both electrodes was

limited by the diffusion of OH$^-$ to the active sites. According to Equation 7,[47]

$$i_p = (2.69 \times 10^5) n^{3/2} A D_o^{1/2} C_o^* v^{1/2} \tag{7}$$

19

where i_p is the peak current, n is the number of electron transferred, A is the electrode area, D_o is the diffusion coefficient, C_o* is the reactant concentration, and v is the scan rate. For comparison, the diffusion coefficients ($D_{Ni(HCO3)2}$ and $D_{NiH-Mn-CO3}$) of the Ni(HCO$_3$)$_2$ and MnCO$_3$ QDs/NiH-Mn-CO$_3$ composite electrodes were calculated from Equation 8, assuming that both electrodes have the same n, A and C_o* values. The diffusion coefficient of the MnCO$_3$ QDs/NiH-Mn-CO$_3$ composite electrode ($D_{Ni-Mn-CO3}$) was 2.5 times larger than that of the Ni(HCO$_3$)$_2$ electrode, indicating the beneficial effect of the shell-needle hybrid electrode. This conclusion was confirmed further by the subsequent galvanostatic charge-discharge tests, as shown in Fig. 8.

$$D_{NiH-Mn-CO3} / D_{Ni(HCO3)2} = [(i_p/v_{1/2})_{NiH-Mn-CO3} / (i_p/v_{1/2})_{Ni(HCO3)2}]^2 =$$

$$(0.02356/0.05072)^2 = 2.354 \qquad (8)$$

As shown in Fig. 78a-b, the charge-discharge measurements of the Ni(HCO$_3$)$_2$ and MnCO$_3$ QDs/NiH-Mn-CO$_3$ composite electrodes were carried out between 0-0.45 V (vs. SCE) at different current densities. The charge/discharge curves are the nonlinear lines, confirming the pseudocapacitance behavior of the electrode materials due to quasi-reversible redox reactions at the electrode-electrolyte interface.[48] The specific capacitance (C_s) of the electrodes was calculated using Equation 9.

$$C_s = I \, \Delta t / m \, \Delta V \qquad (9)$$

where I is the discharge current (A), Δt is the discharge time (s), m is the mass of the electroactive material in the electrode (g), and ΔV is the total potential deviation (V). For the Ni(HCO$_3$)$_2$ electrode, the specific capacitance was calculated to be approximately 1777.5, 1611.0, 1524.4, 1286.0, 1164.4, and 881.1 F g^{-1} at current densities of 3.0, 4.0, 5.0, 8.0, 10.0, and 15.0 A g^{-1}, respectively. A high C_s of 1777.5 F g^{-1} was obtained at a current density of 3 A g^{-1}, which is higher than that reported for Ni oxide/hydroxide electrodes.[49-52] The good performance was attributed to the porous nanostructure of Ni(HCO$_3$)$_2$ on Ni foam. The highly oriented layered thin Ni(HCO$_3$)$_2$ nanosheets were aligned vertically on Ni foam, leading to the resulting well-defined porous nanostructure of Ni(HCO$_3$)$_2$ materials.[53] A large number of Ni(HCO$_3$)$_2$ active sites were exposed to the electrolyte for the Faradaic redox reactions (Equation 5 to 6). In Fig. 8c, the value of C_s decreased with increasing current density. At low current densities, many active sites of the electrodes can access the electrolyte ions, leading to a higher C_s. At a high current density, however, the effective interaction between the ions and electrode was reduced considerably, leading to a lower C_s.[48] The C_s of the Ni(HCO$_3$)$_2$ electrode was reduced to 881.1 F g^{-1} with a retention rate of 49.6% when the current density was increased from 3 to 15 A g^{-1}. For the MnCO$_3$ QDs/NiH-Mn-CO$_3$ composites electrode, the specific capacitance was calculated to be approximately 2622.9, 2289.3, 2157.8, 1909.9, 1774.5, and 1504.5 F g^{-1} at current densities of 3.0, 4.0, 5.0, 8.0, 10.0, and 15.0 A g^{-1}, respectively. Compared to the Ni(HCO$_3$)$_2$ electrode, the C_s value was reduced from

21

2622.9 F g^{-1} (at 3 A g^{-1}) to 1504.5 F g^{-1} (at 15 A g^{-1}), resulting in a retention rate of

57.4%. Obviously, the specific capacitance and high-rate performance of the

MnCO$_3$ QDs/NiH-Mn-CO$_3$ electrode is better than those of Ni(HCO$_3$)$_2$. This was

attributed to the following: (i) The MnCO$_3$ QDs/NiH-Mn-CO$_3$ composite electrode

is much more conducting and electrochemically active than pure Ni(HCO$_3$)$_2$ and the

presence of the well-dispersed high conductive MnCO$_3$ quantum dots, which

shortens the diffusion path of electrolyte ions and improves electron transport from

the active materials to the current collector, as confirmed by the decreasing

equivalent series resistance (Fig. 8e);[54] (ii) the high specific surface area (Fig. 6) and

the well-connected 3D networked structures of nanoneedle-like balls, which reduce

the mass-transfer resistances, accelerate the electrolyte penetration and ion diffusion,

and mitigate the electron hopping between the neighboring nanoparticles;[55] and (iii)

binary metal oxides serving as supercapacitor materials offer richer redox reactions

contributed by both constituent metal ions.[56]

The high life-cycle stability of the electrode is an important factor in the applications

of SCs. The Ni(HCO$_3$)$_2$ and MnCO$_3$ QDs/NiH-Mn-CO$_3$ composites electrodes were

tested for 5000 charge/discharge cycles at a high current density of 15 A g^{-1}, as

shown in Fig. 8d. For MnCO$_3$ QDs/NiH-Mn-CO$_3$ composite electrode, specific

capacitance (C_s) decreased sharply in the first 250 cycles and was stabilized at

1349.6 F g^{-1} after the 650th cycle, which is attributed to the structural instability of

MnCO$_3$ QDs/NiH-Mn-CO$_3$ composites similar to the other metal oxide material in the cycling test.[48] A significant increase in specific capacitance was observed up to the 3100th cycle due to the activation of MnCO$_3$ QDs/NiH-Mn-CO$_3$ composite. Similarly, a decline in C$_s$ was observed in the Ni(HCO$_3$)$_2$ electrode at the first 1000 cycle. Their capacity retention after 5000 cycles at 15 A g^{-1} are 85.5 and 65.8%, respectively. Notably, MnCO$_3$ QDs/NiH-Mn-CO$_3$ shell-needle architecture possesses an intriguing feature which outperforms the Ni(HCO$_3$)$_2$ electrode, indicating that this shell-needle architecture is a promosing design for high-performane supercapacitor applications.

EIS analysis is commonly used to examine the ion transport properties of electrode materials for SCs. To examine the ion transport characteristics of the electrodes, the impedance of the Ni(HCO$_3$)$_2$ and MnCO$_3$ QDs/NiH-Mn-CO$_3$ composites electrodes, as shown in Fig. 8e. For each curve, there was a semicircle intersecting the real axis in the high frequency region. The plot transformed to a vertical line at low frequencies. The semicircle is typical of a *RC* circuit that represents a resistance in parallel with a capacitance.[57] In the low frequency region, the almost complete penetration of ions into the surface or pores of the electrode could be allowed. The vertical line reflects the domination of the capacitive behavior.[58] Fig. 8e shows the proposed equivalent circuit for the measured impedance data, which involves the

23

internal resistance (R_s), double-layer capacitance (C_{dl}) and Faradic charge transfer resistance (R_{ct}), Warburg diffusion element (Z_w), and pseudocapacitance (C_F).[59, 60] Equations 10 and 11 express the overall impedance, Z, of the equivalent circuit in Figure 6b:[61]

$$Z = R_s + \cfrac{1}{j\omega C_{dl} \cfrac{1}{R_{ct} - Z_w}} - j\frac{1}{\omega C_F} \qquad (10)$$

$$Z_w = \frac{W}{\sqrt{j\omega}} \qquad (11)$$

where j is the imaginary unit, ω is the angular frequency (Hz) and W is the Warburg parameter in units of Ω $s^{-1/2}$. This W parameter is an increasing function of the resistance for electrolyte transport in a porous electrode. At sufficiently high frequencies, the overall impedance can be reduced to Equation 12, corresponding to a locus showing a semicircle that intercepts the real axis at R_s and $R_s + R_{ct}$ in the Nyquist plot.[58]

$$Z = R_s + \cfrac{1}{j\omega C_{dl} + \cfrac{1}{R_{ct}}} \qquad (12)$$

As a result, in the high frequency regime, the intercept of the curve at the real axis (Z') equals R_s, which includes the resistance of the electrolyte, Ohmic resistance of the active $Ni(HCO_3)_2$ materials, and contact resistance at the active $Ni(HCO_3)_2$ materials/Ni foam interface. The semicircle, which corresponds to C_{dl} and R_{ct}, showed the charge-transfer process at the working

24

electrode-electrolyte interface. In the low frequency regime, the slope of the curve represents the Warburg resistance (Z_w), which is related to the electrolyte diffusion in the porous electrode and proton diffusion in the $Ni(HCO_3)_2$ materials.

Before the cycling test, the R_s and R_{ct} values of the $Ni(HCO_3)_2$ electrode were 2.985 Ω and 3.278 Ω, respectively. On the other hand, with the $MnCO_3$ QDs/NiH-Mn-CO_3 composites electrode, the values of R_s and R_{ct} decreased to 1.976 Ω and 2.772 Ω, respectively. For the $MnCO_3$ QDs/NiH-Mn-CO_3 composites electrode, R_s consists of the total ohmic resistance of $MnCO_3$ QDs/NiH-Mn-CO_3 composites and Ni foam. The decrease in R_s was attributed to the much more conducting and electrochemically active $MnCO_3$ QDs/NiH-Mn-CO_3 composites electrode than the $Ni(HCO_3)_2$ electrode. The decrease in R_{ct} was attributed to the $MnCO_3$ QDs/NiH-Mn-CO_3 composites materials having a larger porous opening than the $Ni(HCO_3)_2$ materials. Therefore, the electrolyte ions could effectively reach the $MnCO_3$ QDs/NiH-Mn-CO_3 composites surface and react with the active sites. After the 5000th cycle test, the R_s values of the $Ni(HCO_3)_2$ and $MnCO_3$ QDs/NiH-Mn-CO_3 composites electrodes increased, indicating a decrease in the conductivity of the electrodes. The R_{ct} values of the electrodes also increased, which might be due to the morphological changes in the $MnCO_3$ QDs/NiH-Mn-CO_3 composites.

Before the cycle test, the C_{dl} value of the $Ni(HCO_3)_2$ electrode was lower than that of the $MnCO_3$ QDs/NiH-Mn-CO$_3$ composites electrode, suggesting that $MnCO_3$ QDs contributed to charge storage by ion adsorption. For the $Ni(HCO_3)_2$ and $MnCO_3$ QDs/NiH-Mn-CO$_3$ composites electrodes, after 5000 cycles, the C_{dl} value of $Ni(HCO_3)_2$ and $MnCO_3$ QDs/NiH-Mn-CO$_3$ composites electrodes decreased from 0.0241 F to 0.0239 F, and 0.0275 F to 0.0130 F, respectively. This was attributed mainly to the loss of active materials of the electrode. Before the cycle test, the W value of the $Ni(HCO_3)_2$ electrode was higher than that of the $MnCO_3$ QDs/NiH-Mn-CO$_3$ composites electrode, which was attributed to the higher active surface area of the $MnCO_3$ QDs/NiH-Mn-CO$_3$ composites electrode compared to that of $Ni(HCO_3)_2$ resulting in a decrease in the resistance for electrolyte transport in a porous electrode. The C_F value of the $Ni(HCO_3)_2$ electrode was lower than that of the $MnCO_3$ QDs/NiH-Mn-CO$_3$composite electrode, which was attributed to the better conductivity and faster ion transfer efficiency of the $MnCO_3$ QDs/NiH-Mn-CO$_3$ composite electrode than that of the $Ni(HCO_3)_2$ electrode. After the cycle test, for both electrodes, the W values increased and the C_F values decreased. The decrease in C_F was related to the structural stability of the $Ni(HCO_3)_2$ and $MnCO_3$ QDs/NiH-Mn-CO$_3$ composites materials.

The electrochemical properties of 3D porous graphene-Ni foam (G-NF) were measured to examine further the applications of the as-fabricated $MnCO_3$ QDs/NiH-

Mn-CO$_3$//G in an asymmetric supercapacitor (ASC), as shown in Fig. 9a. The as-obtained 3D porous G-NF electrode displayed excellent electric double layer capacitance properties at -1.0 ~ 0.0 V (vs. SCE). The C_s of the 3D porous G-NF electrode, which was calculated from its galvanostatic charge-discharge curves (Fig. 9b), reached 167.8 F g^{-1} at 1 A g^{-1} and 93.0 F g^{-1} at 15 A g^{-1} with a good retention rate of 55.4% (Fig. 9c), which is comparable to those reported previously for graphene-based supercapacitors.[62, 63] EIS showed that G-NF has low R_s and R_{ct} values of 3.418 Ω and 0.693 Ω, respectively (Fig. 9d). These electrochemical behaviors confirmed that the 3D porous G-NF could serve as a negative electrode in ASCs.

To evaluate the performance of the MnCO$_3$ QDs/NiH-Mn-CO$_3$//G in SC applications, an ASC was fabricated with MnCO$_3$ QDs/NiH-Mn-CO$_3$ composites-NF and 3D porous G-NF as the positive and negative electrode, respectively. Based on the C_s values of the MnCO$_3$ QDs/NiH-Mn-CO$_3$ composites electrode and the 3D porous G-NF electrode, as well as the principle of charge balance between the electrodes, the MnCO$_3$ QDs/NiH-Mn-CO$_3$-NF to 3D porous G-NF mass ratio was controlled at approximately 0.31 in the ASC. Fig. 10a shows that the as-fabricated ASC exhibited excellent capacitive behavior at 0~1.8 V with both electric double-layer capacitance and pseudocapacitance. Fig. 10b presents the galvanostatic charge-discharge curves, from which the discharge curve is almost symmetrical with its

corresponding charge counterpart, demonstrating excellent electrochemical reversibility and good Coulombic efficiency.[64] The C_s values were calculated to be 129.0, 102.3, 87.1, 80.9, 74.7, 59.7, 52.2 and 39.7 F g^{-1} at current densities of 1, 2, 3, 4, 5, 8, 10, and 15 A g^{-1}, respectively (based on the total mass of the active material in the positive and negative electrodes) (Fig. 10c). Based on these C_s values, the highest energy density of the asymmetric supercapacitor (Fig. 10e) was calculated to be 58.1 Wh kg^{-1} at a power density of 900 W kg^{-1}. At a high discharge current of 15 A g^{-1}, the energy density was reduced to 17.9 Wh kg^{-1} at a power density of 13.5 kW kg^{-1}. The results show that the ASC achieved a higher energy density than the other devices, such as Ni(OH)$_2$@3D Ni//AC (21.8 Wh kg^{-1} at 660 W kg^{-1}),[65] NiCo LDH-Zn$_2$SnO4//AC (23.7 Wh kg^{-1} at 284.2 W kg^{-1})[66] and NiCo$_2$O$_4$@MnO$_2$-NF//AC (28 Wh kg^{-1} at 400 W kg^{-1}), NiO//Carbon,[67] MnO$_2$//Carbon,[63] Ni(OH)$_2$//Carbon,[68] and N-RGO//N-RGO.[69] Moreover, the energy and power densities of MnCO$_3$ QDs/NiH-Mn-CO$_3$//G outperformed those of most nickel or cobalt oxides/hydroxides as well as other typical material-based ASCs (Table S2, Supporting Information). The ultrahigh energy density of the device was attributed to the good energy storage ability of the binder-free MnCO$_3$ QDs/NiH-Mn-CO$_3$//G electrode. The galvanostatic charge-discharge test was also carried out to evaluate the durability of the as-fabricated ASC with 0-1.8 V for 10000 cycles at a current density of 5 A g^{-1}. As shown in Figure 9d, the initial specific capacitance of the ASC was 74.4 F g^{-1}, which

then stabilized at 68.0 F g^{-1} (with a retention rate of 91.3%) after 10000 cycles, which is comparable to those of the ASCs.[62, 70, 71]

Conclusions

A 3D open structure composed of $MnCO_3$ QDs/$Ni(HCO_3)_2$-$MnCO_3$ shell-needle composite was grown on macro-porous nickel foam by a facile and efficient one-step hydrothermal method. $MnCO_3$ QDs with a mean diameter of ~1.2 nm were self-assembled due to different Ni and Mn adtom mobilities on the surface of NiH-Mn-CO_3 nanoneedles. The as-obtained $MnCO_3$ QDs/NiH-Mn-CO_3 nanostructure was used directly as a binder-free electrode in a supercapacitor, which showed a remarkable high specific capacitance (2622.9 F g^{-1} at 3 A g^{-1}) and good capacitance retention rate. The proposed $MnCO_3$ QDs/Ni-Mn-CO_3//G asymmetric supercapacitor exhibited a higher energy density of 58.1 Wh kg^{-1} at a power density of 900 W kg^{-1} based on the total mass of active materials compared to those of most previously reported nickel or manganese oxide/hydroxide-based asymmetric supercapacitors as well as other typical asymmetric supercapacitors. The superior electrochemical performance is attributed to the presence of high surface area core-shell nanostructure, the well dispersed high conductive $MnCO_3$ quantum dots as well as the synergetic effect between multiple transition metal ions. This work shows that the as-obtained $MnCO_3$ QDs/NiH-Mn-CO_3 shell-needle composite

nanostructures are promising electrode materials for the further development of

high-performance energy-storage devices.

Acknowledgements

References

1.	Lee, J.; Urban, A.; Li, X.; Su, D.; Hautier, G.; Ceder, G., Unlocking the Potential of Cation-Disordered Oxides for Rechargeable Lithium Batteries. *Science* 2014, 343, 519-522.

2.	Simon, P.; Gogotsi, Y., Materials for electrochemical capacitors. *Nat Mater* 2008, 7, 845-854.

3.	Gao, P. C.; Tsai, W. Y.; Daffos, B.; Taberna, P. L.; Perez, C. R.; Gogotsi, Y.; Simon, P.; Favier, F., Graphene-like carbide derived carbon for high-power supercapacitors. *Nano Energy* 2015, 12, 197-206.

4.	Chmiola, J.; Largeot, C.; Taberna, P. L.; Simon, P.; Gogotsi, Y., Monolithic Carbide-Derived Carbon Films for Micro-Supercapacitors. *Science* 2010, 328, 480-483.

5.	Hatzell, K. B.; Fan, L.; Beidaghi, M.; Boota, M.; Pomerantseva, E.; Kumbur, E. C.; Gogotsi, Y., Composite Manganese Oxide Percolating Networks As a Suspension Electrode for an Asymmetric Flow Capacitor. *Acs Appl Mater Inter* 2014, 6, 8886-8893.

6.	Simon, P.; Gogotsi, Y., Capacitive Energy Storage in Nanostructured Carbon-Electrolyte Systems. *Accounts Chem Res* 2013, 46, 1094-1103.

7.	Zhou, Q.; Zhao, Z. B.; Wang, Z. Y.; Dong, Y. F.; Wang, X. Z.; Gogotsi, Y.; Qiu, J. S., Low temperature plasma synthesis of mesoporous Fe3O4 nanorods grafted on reduced graphene oxide for high performance lithium storage. *Nanoscale* 2014, 6, 2286-2291.

8.	Anasori, B.; Beidaghi, M.; Gogotsi, Y., Graphene - transition metal oxide hybrid materials Hybrid structures for energy storage. *Mater Today* 2014, 17, 253-254.

9.	Wang, C. D.; Xu, J. L.; Yuen, M. F.; Zhang, J.; Li, Y. Y.; Chen, X. F.; Zhang, W. J., Hierarchical Composite Electrodes of Nickel Oxide Nanoflake 3D Graphene for High-Performance Pseudocapacitors. *Adv Funct Mater* 2014, 24, 6372-6380.

10.	Huang, M.; Zhang, Y. X.; Li, F.; Zhang, L. L.; Ruoff, R. S.; Wen, Z. Y.; Liu, Q., Self-Assembly of Mesoporous Nanotubes Assembled from Interwoven Ultrathin Birnessite-type MnO2 Nanosheets for Asymmetric Supercapacitors. *Sci Rep-Uk* 2014, 4.

11.	Meher, S. K.; Justin, P.; Rao, G. R., Nanoscale morphology dependent pseudocapacitance of NiO: Influence of intercalating anions during synthesis. *Nanoscale* 2011, 3, 683-692.

12.	Justin, P.; Meher, S. K.; Rao, G. R., Tuning of Capacitance Behavior of NiO Using Anionic, Cationic, and Nonionic Surfactants by Hydrothermal Synthesis. *J Phys Chem C* 2010, 114, 5203-5210.

13.	How, G. T. S.; Pandikumar, A.; Ming, H. N.; Ngee, L. H., Highly exposed {001} facets of titanium dioxide modified with reduced graphene oxide for dopamine sensing. *Sci Rep-Uk* 2014, 4.

14.   Chen, H.; Hu, L. F.; Yan, Y.; Che, R. C.; Chen, M.; Wu, L. M., One-Step Fabrication of Ultrathin Porous Nickel Hydroxide-Manganese Dioxide Hybrid Nanosheets for Supercapacitor Electrodes with Excellent Capacitive Performance. *Adv Energy Mater* 2013, 3, 1636-1646.

15.   Liu, J. P.; Jiang, J.; Bosman, M.; Fan, H. J., Three-dimensional tubular arrays of MnO2-NiO nanoflakes with high areal pseudocapacitance. *J Mater Chem* 2012, 22, 2419-2426.

16.   Wan, H. Z.; Jiang, J. J.; Ruan, Y. J.; Yu, J. W.; Zhang, L.; Chen, H. C.; Miao, L.; Bie, S. W., Direct Formation of Hedgehog-Like Hollow Ni-Mn Oxides and Sulfides for Supercapacitor Electrodes. *Part Part Syst Char* 2014, 31, 857-862.

17.   Latorre-Sanchez, M.; Atienzar, P.; Abellan, G.; Puche, M.; Fornes, V.; Ribera, A.; Garcia, H., The synthesis of a hybrid graphene-nickel/manganese mixed oxide and its performance in lithium-ion batteries. *Carbon* 2012, 50, 518-525.

18.   Zhao, J. W.; Chen, J.; Xu, S. M.; Shao, M. F.; Zhang, Q.; Wei, F.; Ma, J.; Wei, M.; Evans, D. G.; Duan, X., Hierarchical NiMn Layered Double Hydroxide/Carbon Nanotubes Architecture with Superb Energy Density for Flexible Supercapacitors. *Adv Funct Mater* 2014, 24, 2938-2946.

19.   Dubal, D. P.; Gomez-Romero, P.; Sankapal, B. R.; Holze, R., Nickel cobaltite as an emerging material for supercapacitors: An overview. *Nano Energy* 2015, 11, 377-399.

20.   Pang, H.; Deng, J. W.; Wang, S. M.; Li, S. J.; Du, J. M.; Chen, J.; Zhang, J. S., Facile synthesis of porous nickel manganite materials and their morphology effect on electrochemical properties. *Rsc Adv* 2012, 2, 5930-5934.

21.   Jiang, H.; Li, C. Z.; Sun, T.; Ma, J., High-performance supercapacitor material based on Ni(OH)(2) nanowire-MnO2 nanoflakes core-shell nanostructures. *Chem Commun* 2012, 48, 2606-2608.

22.   Rusi; Majid, S. R., High performance super-capacitive behaviour of deposited manganese oxide/nickel oxide binary electrode system. *Electrochim Acta* 2014, 138, 1-8.

23.   Sun, J. Q.; Li, W. Y.; Zhang, B. J.; Li, G.; Jiang, L.; Chen, Z. G.; Zou, R. J.; Hu, J. Q., 3D core/shell hierarchies of MnOOH ultrathin nanosheets grown on NiO nanosheet arrays for high-performance supercapacitors. *Nano Energy* 2014, 4, 56-64.

24.   Peng, C. X.; Chen, B. D.; Qin, Y.; Yang, S. H.; Li, C. Z.; Zuo, Y. H.; Liu, S. Y.; Yang, J. H., Facile Ultrasonic Synthesis of CoO Quantum Dot/Graphene Nanosheet Composites with High Lithium Storage Capacity. *Acs Nano* 2012, 6, 1074-1081.

25.   Xia, H.; Hong, C. Y.; Li, B.; Zhao, B.; Lin, Z. X.; Zheng, M. B.; Savilov, S. V.; Aldoshin, S. M., Facile Synthesis of Hematite Quantum-Dot/Functionalized Graphene-Sheet Composites as Advanced Anode Materials for Asymmetric Supercapacitors. *Adv Funct Mater* 2015, 25, 627-635.

26.   Mo, R. W.; Lei, Z. Y.; Sun, K. N.; Rooney, D., Facile Synthesis of Anatase TiO2 Quantum- Dot/GrapheneNanosheet Composites with Enhanced

Electrochemical Performance for Lithium-Ion Batteries. *Adv Mater* 2014, 26, 2084-2088.

27.   Heiss, M.; Fontana, Y.; Gustafsson, A.; Wust, G.; Magen, C.; O'Regan, D. D.; Luo, J. W.; Ketterer, B.; Conesa-Boj, S.; Kuhlmann, A. V.; Houel, J.; Russo-Averchi, E.; Morante, J. R.; Cantoni, M.; Marzari, N.; Arbiol, J.; Zunger, A.; Warburton, R. J.; Morral, A. F. I., Self-assembled quantum dots in a nanowire system for quantum photonics. *Nat Mater* 2013, 12, 439-444.

28.   Tsang, C. H. A.; Hui, K. N.; Hui, K. S.; Ren, L., Deposition of Pd/graphene aerogel on nickel foam as a binder-free electrode for direct electro-oxidation of methanol and ethanol. *J Mater Chem A* 2014, 2, 17986-17993.

29.   Hu, M. C.; Hui, K. S.; Hui, K. N., Role of graphene in MnO2/graphene composite for catalytic ozonation of gaseous toluene. *Chem Eng J* 2014, 254, 237-244.

30.   Zhao, H.; Hui, K. S.; Hui, K. N., Synthesis of nitrogen-doped multilayer graphene from milk powder with melamine and their application to fuel cells. *Carbon* 2014, 76, 1-9.

31.   Xiaogang Han, M. R. F., Fei Shen, Yu-Chen Chen, Yuanyuan Li, Caroline J. Campbel,Jiaqi Dai, Xiaofeng Yang, Jae-Woo Kim, Yunlong Liao, John W. Connell, Veronica Barone, Zhongfang Chen, Yi Lin and Liangbing Hu, Scalable Holey Graphene Synthesis and Dense Electrode Fabrication toward High-Performance Ultracapacitors. *ACSNANO* 2014, 8.

32.   Chen, L. F.; Huang, Z. H.; Liang, H. W.; Guan, Q. F.; Yu, S. H., Bacterial-Cellulose-Derived Carbon Nanofiber@MnO2 and Nitrogen-Doped Carbon Nanofiber Electrode Materials: An Asymmetric Supercapacitor with High Energy and Power Density. *Adv Mater* 2013, 25, 4746-4752.

33.   Xiaowei Yang, C. C., Yufei Wang, Ling Qiu, Dan Li, Liquid-Mediated Dense Integration of Graphene Materials for Compact Capacitive Energy Storage. *Science* 2013, 341.

34.   Yan, Y. N.; Cheng, G.; Wang, P.; He, D. N.; Chen, R., Facile hydrothermal selective fabrication of Ni(OH)(2) and Ni(HCO3)(2) nanoparticulates and their electrochemical performances. *Rsc Adv* 2014, 4, 49303-49307.

35.   Cai, S. X.; Zhang, D. S.; Shi, L. Y.; Xu, J.; Zhang, L.; Huang, L.; Li, H. R.; Zhang, J. P., Porous Ni-Mn oxide nanosheets in situ formed on nickel foam as 3D hierarchical monolith de-NOx catalysts. *Nanoscale* 2014, 6, 7346-7353.

36.   Liu, Y.; Xu, J.; Li, H. R.; Cai, S. X.; Hu, H.; Fang, C.; Shi, L. Y.; Zhang, D. S., Rational design and in situ fabrication of MnO2@NiCo2O4 nanowire arrays on Ni foam as high-performance monolith de-NOx catalysts. *J Mater Chem A* 2015, 3, 11543-11553.

37.   Xu, K. B.; Li, W. Y.; Liu, Q.; Li, B.; Liu, X. J.; An, L.; Chen, Z. G.; Zou, R. J.; Hu, J. Q., Hierarchical mesoporous NiCo2O4@MnO2 core-shell nanowire arrays on nickel foam for aqueous asymmetric supercapacitors. *J Mater Chem A* 2014, 2, 4795-4802.

33

38.   Liu, F. D.; He, H.; Ding, Y.; Zhang, C. B., Effect of manganese substitution on the structure and activity of iron titanate catalyst for the selective catalytic reduction of NO with NH3. *Appl Catal B-Environ* 2009, 93, 194-204.

39.   Zhang, Y.; Pu, X. L.; Yang, Y. C.; Zhu, Y. R.; Hou, H. R.; Jing, M. J.; Yang, X. M.; Chena, J.; Ji, X. B., An electrochemical investigation of rutile TiO2 microspheres anchored by nanoneedle clusters for sodium storage. *Phys Chem Chem Phys* 2015, 17, 15764-15770.

40.   Zhang, G. Q.; Lou, X. W., Controlled Growth of NiCo2O4 Nanorods and Ultrathin Nanosheets on Carbon Nanofibers for High-performance Supercapacitors. *Sci Rep-Uk* 2013, 3, 1470.

41.   Wu, J.; Mi, R.; Li, S.; Guo, P.; Mei, J.; Liu, H.; Lau, W. M.; Liu, L. M., Hierarchical three-dimensional NiCo2O4 nanoneedle arrays supported on Ni foam for high-performance supercapacitors. *Rsc Adv* 2015, 5, 25304-25311.

42.   Wang, W.; Guo, S. R.; Penchev, M.; Ruiz, I.; Bozhilov, K. N.; Yan, D.; Ozkan, M.; Ozkan, C. S., Three dimensional few layer graphene and carbon nanotube foam architectures for high fidelity supercapacitors. *Nano Energy* 2013, 2, 294-303.

43.   Lin, T. W.; Dai, C. S.; Hung, K. C., High Energy Density Asymmetric Supercapacitor Based on NiOOH/Ni3S2/3D Graphene and Fe3O4/Graphene Composite Electrodes. *Sci Rep-Uk* 2014, 4, 7274.

44.   Wu, Z.; Huang, X. L.; Wang, Z. L.; Xu, J. J.; Wang, H. G.; Zhang, X. B., Electrostatic Induced Stretch Growth of Homogeneous beta-Ni(OH)(2) on Graphene with Enhanced High-Rate Cycling for Supercapacitors. *Sci Rep-Uk* 2014, 4, 3669.

45.   Zheng, F. L.; Li, G. R.; Ou, Y. N.; Wang, Z. L.; Su, C. Y.; Tong, Y. X., Synthesis of hierarchical rippled Bi2O3 nanobelts for supercapacitor applications. *Chem Commun* 2010, 46, 5021-5023.

46.   Meher, S. K.; Justin, P.; Rao, G. R., Microwave-Mediated Synthesis for Improved Morphology and Pseudocapacitance Performance of Nickel Oxide. *Acs Appl Mater Inter* 2011, 3, 2063-2073.

47.   Li, L. L.; Zhang, W. M.; Yuan, Q.; Li, Z. X.; Fang, C. J.; Sun, L. D.; Wan, L. J.; Yan, C. H., Room Temperature Ionic Liquids Assisted Green Synthesis of Nanocrystalline Porous SnO2 and Their Gas Sensor Behaviors. *Cryst Growth Des* 2008, 8, 4165-4172.

48.   Zhang, L. J.; Wang, J.; Zhu, J. J.; Zhang, X. G.; Hui, K. S.; Hui, K. N., 3D porous layered double hydroxides grown on graphene as advanced electrochemical pseudocapacitor materials. *J Mater Chem A* 2013, 1, 9046-9053.

49.   Huang, M.; Li, F.; Ji, J. Y.; Zhang, Y. X.; Zhao, X. L.; Gao, X., Facile synthesis of single-crystalline NiO nanosheet arrays on Ni foam for high-performance supercapacitors. *Crystengcomm* 2014, 16, 2878-2884.

50.   Gund, G. S.; Dubal, D. P.; Jambure, S. B.; Shinde, S. S.; Lokhande, C. D., Temperature influence on morphological progress of Ni(OH)(2) thin films and its

subsequent effect on electrochemical supercapacitive properties. *J Mater Chem A* 2013, 1, 4793-4803.

51.   Yang, S. B.; Wu, X. L.; Chen, C. L.; Dong, H. L.; Hu, W. P.; Wang, X. K., Spherical alpha-Ni(OH)(2) nanoarchitecture grown on graphene as advanced electrochemical pseudocapacitor materials. *Chem Commun* 2012, 48, 2773-2775.

52.   Ji, J. Y.; Zhang, L. L.; Ji, H. X.; Li, Y.; Zhao, X.; Bai, X.; Fan, X. B.; Zhang, F. B.; Ruoff, R. S., Nanoporous Ni(OH) Thin Film on 3D Ultrathin-Graphite Foam for Asymmetric Supercapacitor. *Acs Nano* 2013, 7, 6237-6243.

53.   Wang, J.; Song, Y. C.; Li, Z. S.; Liu, Q.; Zhou, J. D.; Jing, X. Y.; Zhang, M. L.; Jiang, Z. H., In Situ Ni/Al Layered Double Hydroxide and Its Electrochemical Capacitance Performance. *Energ Fuel* 2010, 24, 6463-6467.

54.   Tarasevich, B. N. E. M. R., *Elsevier* 1982, P. 227.

55.   Hu, Y. F.; Zhou, J.; Yeh, P. H.; Li, Z.; Wei, T. Y.; Wang, Z. L., Supersensitive, Fast-Response Nanowire Sensors by Using Schottky Contacts. *Adv Mater* 2010, 22, 3327-3332.

56.   Wang, H. L.; Gao, Q. M.; Jiang, L., Facile Approach to Prepare Nickel Cobaltite Nanowire Materials for Supercapacitors. *Small* 2011, 7, 2454-2459.

57.   Nian, Y. R.; Teng, H. S., Influence of surface oxides on the impedance behavior of carbonbased electrochemical capacitors. *J Electroanal Chem* 2003, 540, 119-127.

58.   Wang, K. P.; Teng, H. S., Structural feature and double-layer capacitive performance of porous carbon powder derived from polyacrylonitrile-based carbon fiber. *J Electrochem Soc* 2007, 154, A993-A998.

59.   Ghodbane, O.; Louro, M.; Coustan, L.; Patru, A.; Favier, F., Microstructural and Morphological Effects on Charge Storage Properties in MnO2-Carbon Nanofibers Based Supercapacitors. *J Electrochem Soc* 2013, 160, A2315-A2321.

60.   Sen, P.; De, A., Electrochemical performances of poly(3,4-ethylenedioxythiophene)-NiFe2O4 nanocomposite as electrode for supercapacitor. *Electrochim Acta* 2010, 55, 4677-4684.

61.   Huang, C. W.; Teng, H. S., Influence of carbon nanotube grafting on the impedance behavior of activated carbon capacitors. *J Electrochem Soc* 2008, 155, A739-A744.

62.   Wu, Z. S.; Winter, A.; Chen, L.; Sun, Y.; Turchanin, A.; Feng, X. L.; Mullen, K., Three-Dimensional Nitrogen and Boron Co-doped Graphene for High-Performance All-Solid-State Supercapacitors. *Adv Mater* 2012, 24, 5130-5135.

63.   Huang, J. C.; Xu, P. P.; Cao, D. X.; Zhou, X. B.; Yang, S. N.; Li, Y. J.; Wang, G. L., Asymmetric supercapacitors based on beta-Ni(OH)(2) nanosheets and activated carbon with high energy density. *J Power Sources* 2014, 246, 371-376.

64.   Su, Y. Z.; Xiao, K.; Li, N.; Liu, Z. Q.; Qiao, S. Z., Amorphous Ni(OH)(2) @ three-dimensional Ni core-shell nanostructures for high capacitance pseudocapacitors and asymmetric supercapacitors. *J Mater Chem A* 2014, 2, 13845-13853.

65. Wang, X.; Sumboja, A.; Lin, M. F.; Yan, J.; Lee, P. S., Enhancing electrochemical reaction sites in nickel-cobalt layered double hydroxides on zinc tin oxide nanowires: a hybrid material for an asymmetric supercapacitor device. *Nanoscale* 2012, 4, 7266-7272.

66. Wang, D. W.; Li, F.; Cheng, H. M., Hierarchical porous nickel oxide and carbon as electrode materials for asymmetric supercapacitor. *J Power Sources* 2008, 185, 1563-1568.

67. Qu, Q. T.; Zhang, P.; Wang, B.; Chen, Y. H.; Tian, S.; Wu, Y. P.; Holze, R., Electrochemical Performance of MnO2 Nanorods in Neutral Aqueous Electrolytes as a Cathode for Asymmetric Supercapacitors. *J Phys Chem C* 2009, 113, 14020-14027.

68. Lee, Y. H.; Chang, K. H.; Hu, C. C., Differentiate the pseudocapacitance and double-layer capacitance contributions for nitrogen-doped reduced graphene oxide in acidic and alkaline electrolytes. *J Power Sources* 2013, 227, 300-308.

69. Wang, X.; Yan, C. Y.; Sumboja, A.; Lee, P. S., High performance porous nickel cobalt oxide nanowires for asymmetric supercapacitor. *Nano Energy* 2014, 3, 119-126.

70. Tang, Z.; Tang, C. H.; Gong, H., A High Energy Density Asymmetric Supercapacitor from Nano-architectured Ni(OH)2/Carbon Nanotube Electrodes. *Adv Funct Mater* 2012, 22, 1272-1278.

71. Park, S.; An, J. H.; Piner, R. D.; Jung, I.; Yang, D. X.; Velamakanni, A.; Nguyen, S. T.; Ruoff, R. S., Aqueous Suspension and Characterization of Chemically Modified Graphene Sheets. *Chem Mater* 2008, 20, 6592-6594.
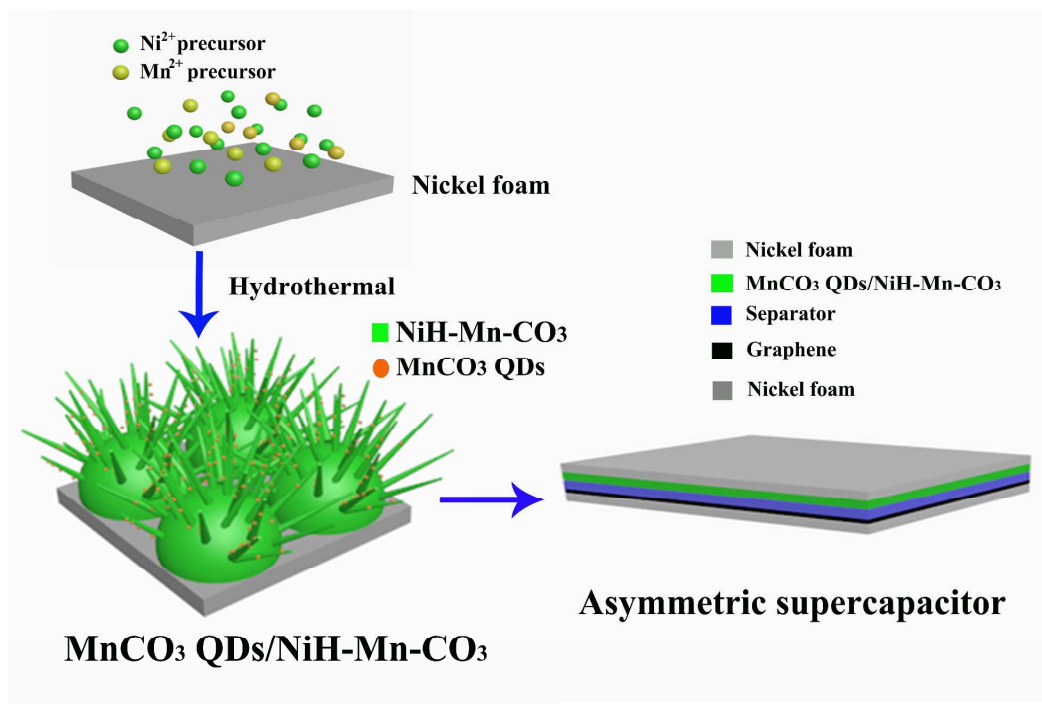
Scheme 1. Schematic diagram of the synthesis process of MnCO$_3$ QDs/NiH-Mn-CO$_3$//graphene asymmetric supercapacitor.
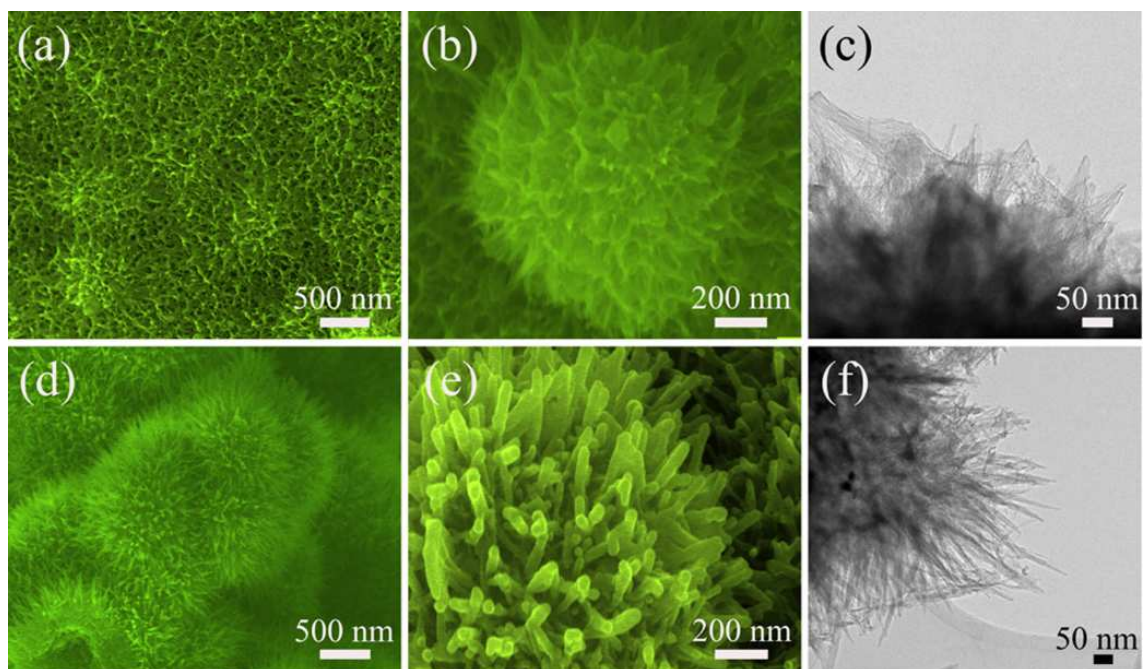
Fig.1 (a) and (b) Field-emission scanning electron microscopy (FESEM) images of the as-obtained porous $Ni(HCO_3)_2$ nanosheet arrays grown uniformly on 3D macroporous Ni foam, (c) low magnification TEM image of the porous $Ni(HCO_3)_2$ nanosheet arrays; (d) and (e) FESEM images of the as-obtained hierarchical porous $MnCO_3$ QDs/NiH-Mn-CO_3 composites grown uniformly on Ni foam, (f) low magnification TEM image of the $MnCO_3$ QDs/NiH-Mn-CO_3 composites showing needle arrays.
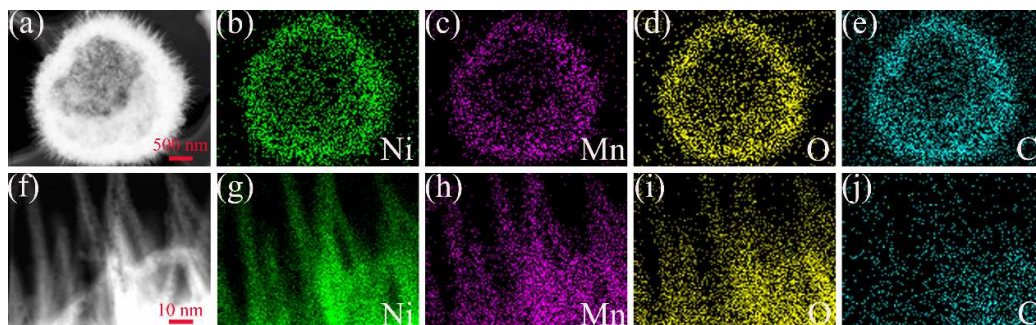
Fig. 2 Microstructure and chemistry of the MnCO$_3$ QDs/NiH-Mn-CO$_3$ composites.
(a) Low magnification TEM image of hedgehog-like MnCO$_3$ QDs/Ni-Mn-CO$_3$
composites. The EDS mapping of (b) Ni, (c) Mn, (d) O, (e) C; (f) High
magnification TEM image of nanoneedle on hedgehog-like MnCO$_3$ QDs/NiH-Mn-
CO$_3$ composites and EDS mapping of (g) Ni, (h) Mn, (i) O, (j) C.
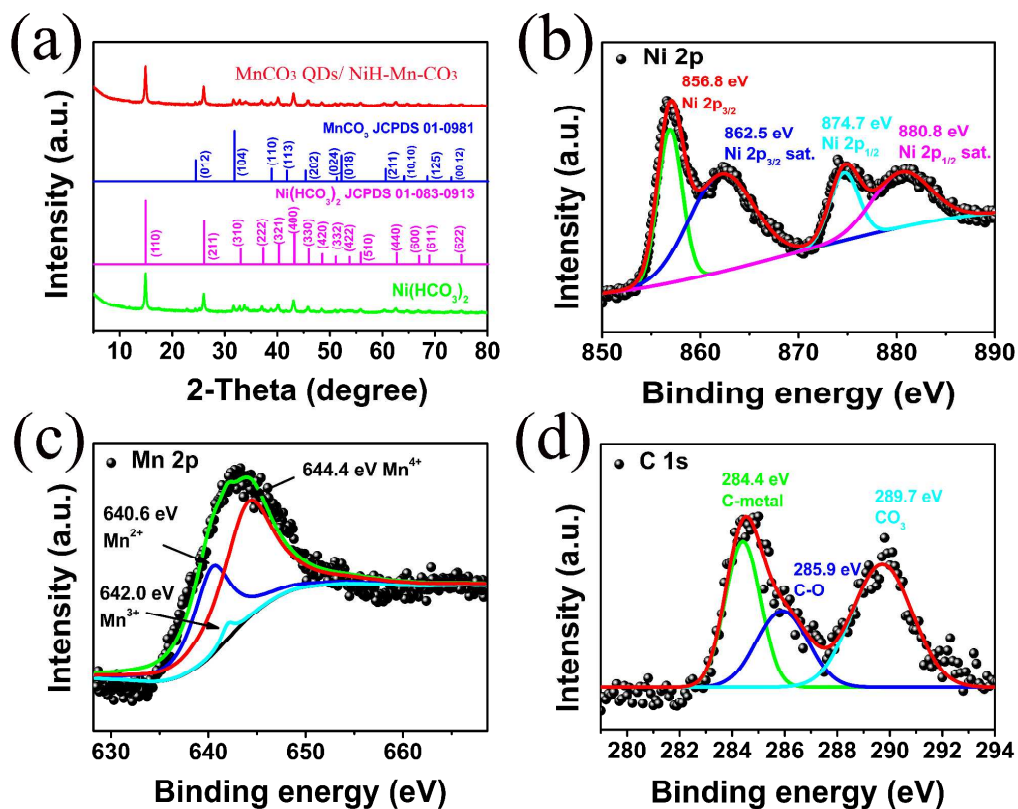
Fig. 3 (a) XRD analysis of the $Ni(HCO_3)_2$ nanosheet and $MnCO_3$ QDs/NiH-Mn-CO$_3$ composites. XPS spectra of $MnCO_3$ QDs/Ni-Mn-CO$_3$ composites (b) Mn 2p, (c) Ni 2p and (d) C 1s.
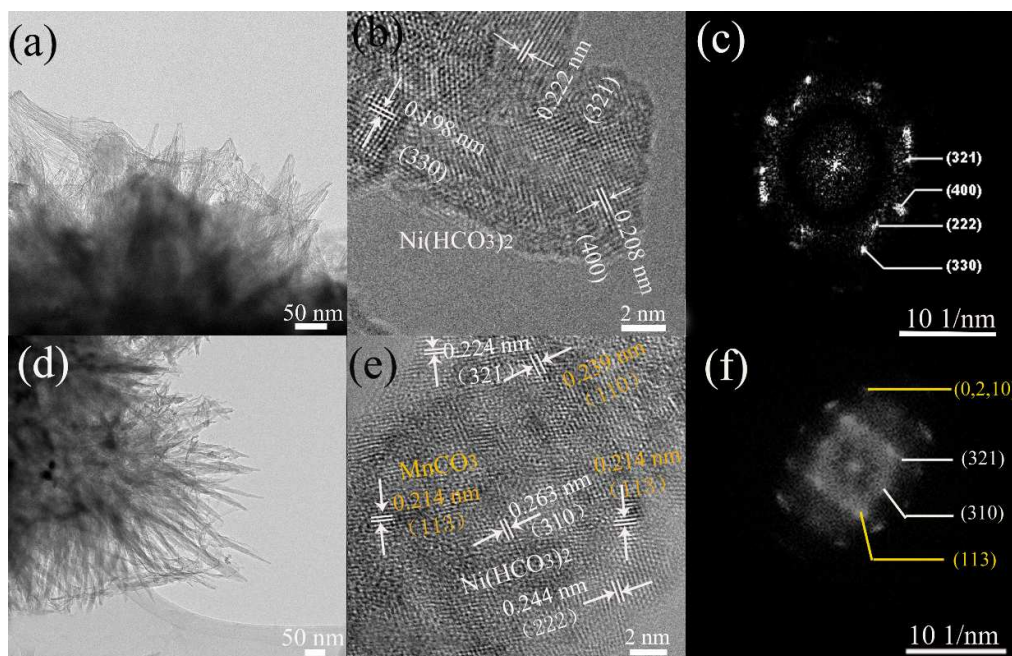
Fig. 4 (a) Low magnification TEM image, (b) HRTEM image, and (c) FFT pattern of the HRTEM image of the Ni(HCO$_3$)$_2$ nanosheet; (d) low magnification TEM image, (e) HRTEM image, and (f) FFT pattern of the HRTEM image of the MnCO$_3$ QDs/NiH-Mn-CO$_3$ composites.
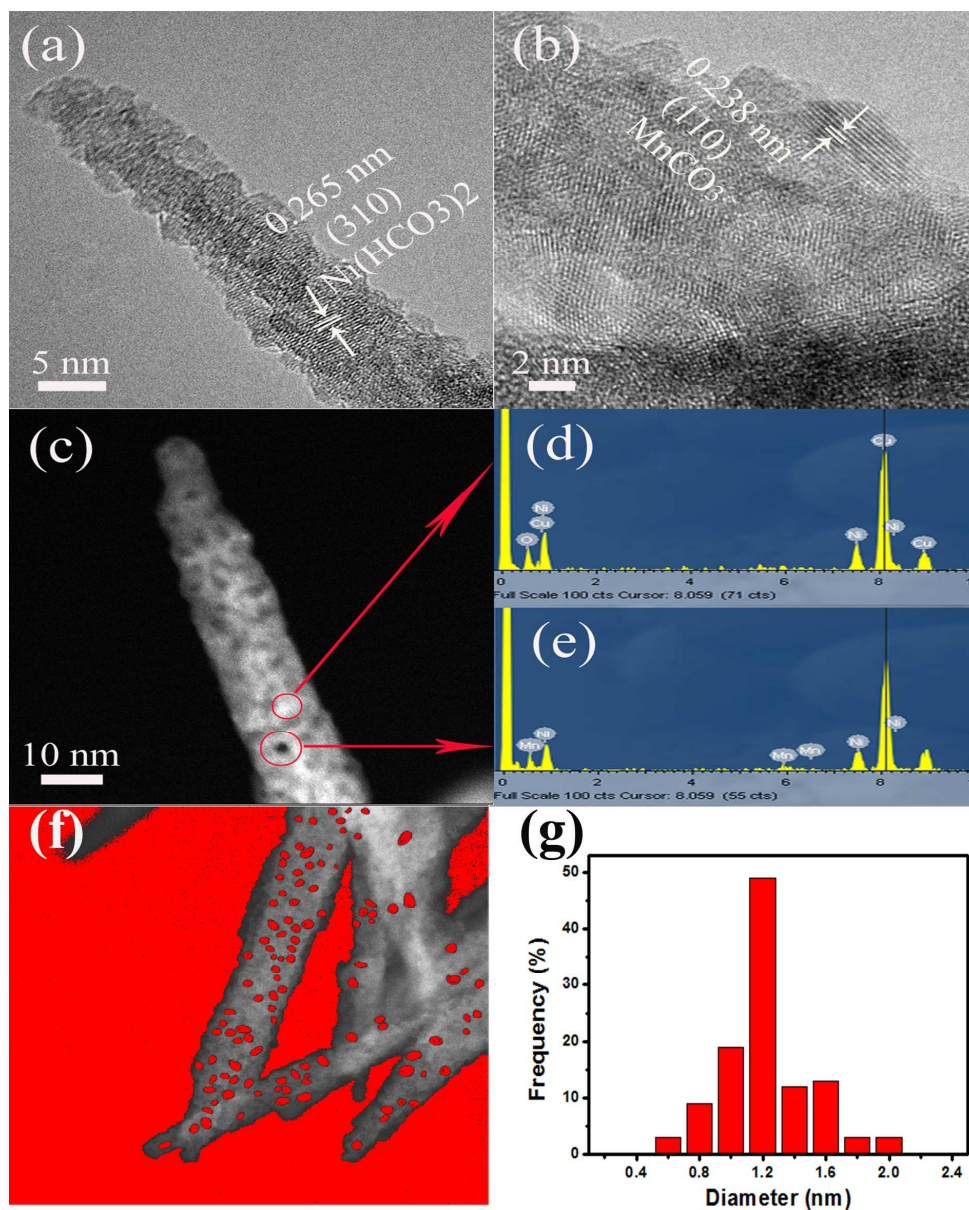
Fig. 5 (a) and (b) HRTEM image of a $MnCO_3$ QDs/NiH-Mn-CO_3 nanoneedle. (c) ADF-STEM image of $MnCO_3$ QDs/Ni-Mn-CO_3 composites and its selected-area EDX spectrum are shown in (d) and (e). (f) ADF-STEM image of $MnCO_3$ QDs/NiH-Mn-CO_3 composites and (g) size distribution of $MnCO_3$ QDs.
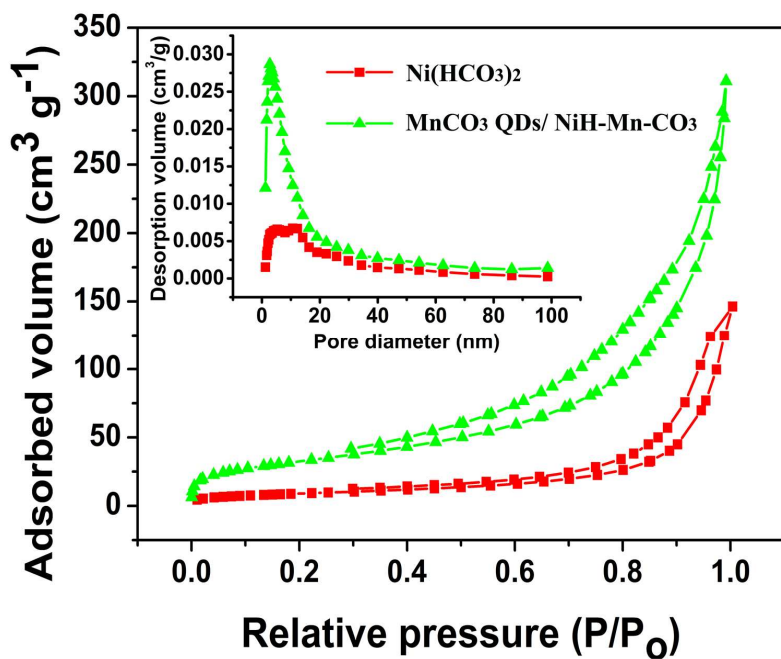
Fig. 6 N_2 adsorption-desorption isotherm loop and pore size distribution data (inset) of the $Ni(HCO_3)_2$ nanosheet (red solid square) and $MnCO_3$ QDs/NiH-Mn-CO$_3$ composites (green solid triangle).
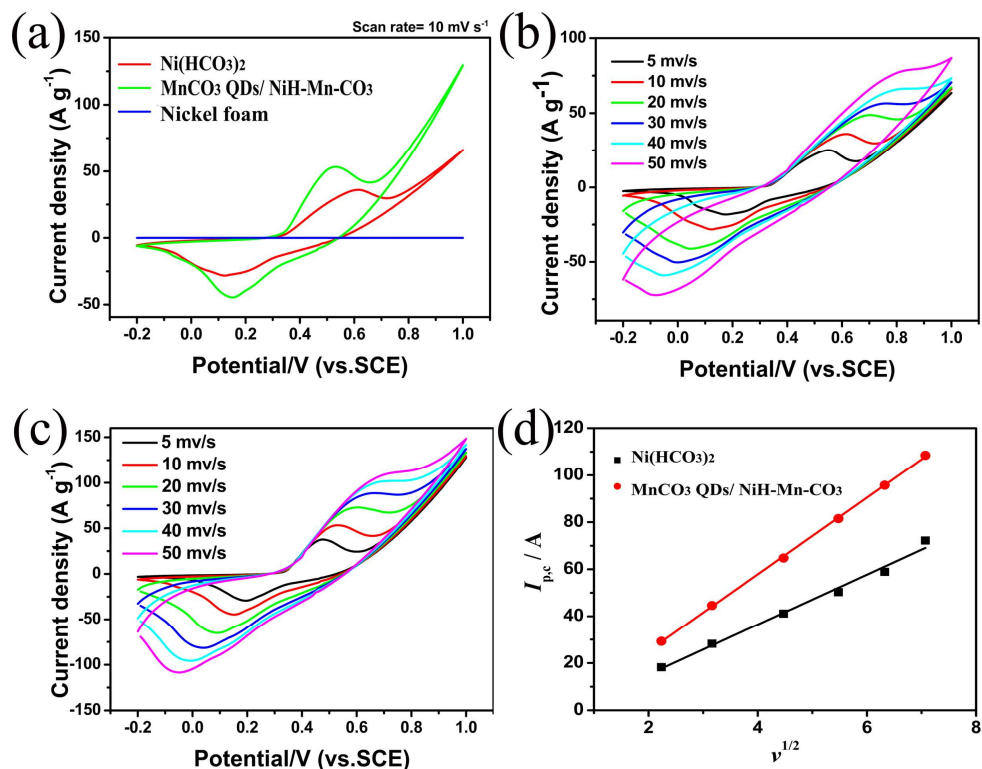
Fig. 7 Comparison of the CV curves of the $Ni(HCO_3)_2$ nanosheet and $MnCO_3$ QDs/NiH-Mn-CO_3 composites electrodes at a scan rate of 10 mV s^{-1}. (b) CV curves of the $Ni(HCO_3)_2$ electrode at different scan rates. (c) CV curves of the $MnCO_3$ QDs/NiH-Mn-CO_3 composites electrode at different scan rates. (d) Relationship between the cathodic peak current and square root of the scan rate for $Ni(NCO_3)$ (black solid square) and $MnCO_3$ QDs/NiH-Mn-CO_3 composites (red solid circle) electrodes.
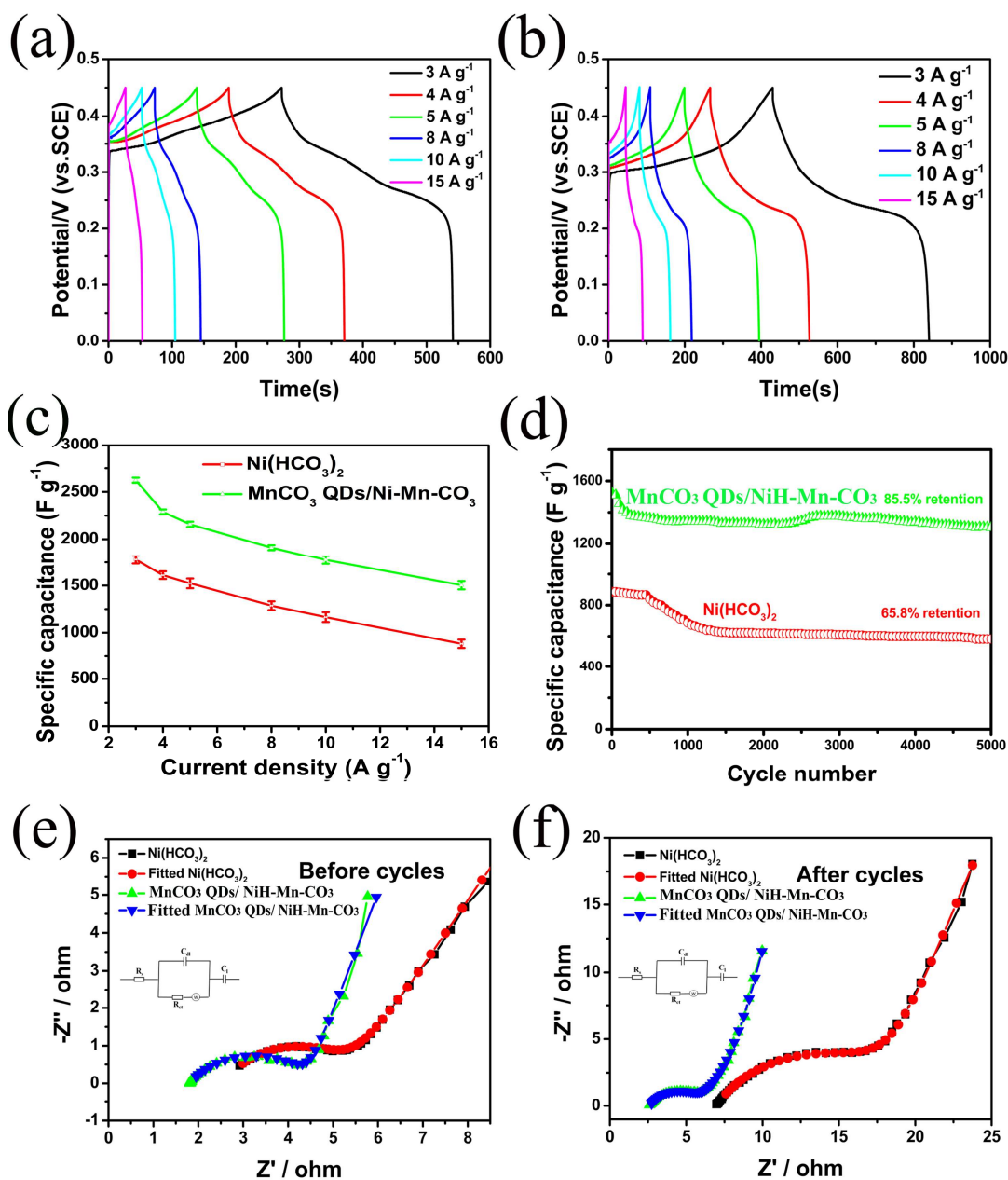
Fig. 8 Electrochemical performance of Ni(HCO$_3$)$_2$ and MnCO$_3$ QDs/NiH-Mn-CO$_3$ composites electrodes before cycling tests. Galvanostatic charge-discharge curves of (a) Ni(HCO$_3$)$_2$ and (b) MnCO$_3$ QDs/NiH-Mn-CO$_3$ composites electrode. (c) Comparison of the specific capacitances of Ni(HCO$_3$)$_2$ and MnCO$_3$ QDs/NiH-Mn-CO$_3$ composites electrodes at different current densities. (d) Cycling performance of Ni(HCO$_3$)$_2$ and MnCO$_3$ QDs/NiH-Mn-CO$_3$ composites electrodes at a current density of 15 A/g. (e) EIS spectrum of the Ni(HCO$_3$)$_2$ and MnCO$_3$ QDs/NiH-Mn-CO$_3$ composites electrodes (e) before and (f) after cycling tests.
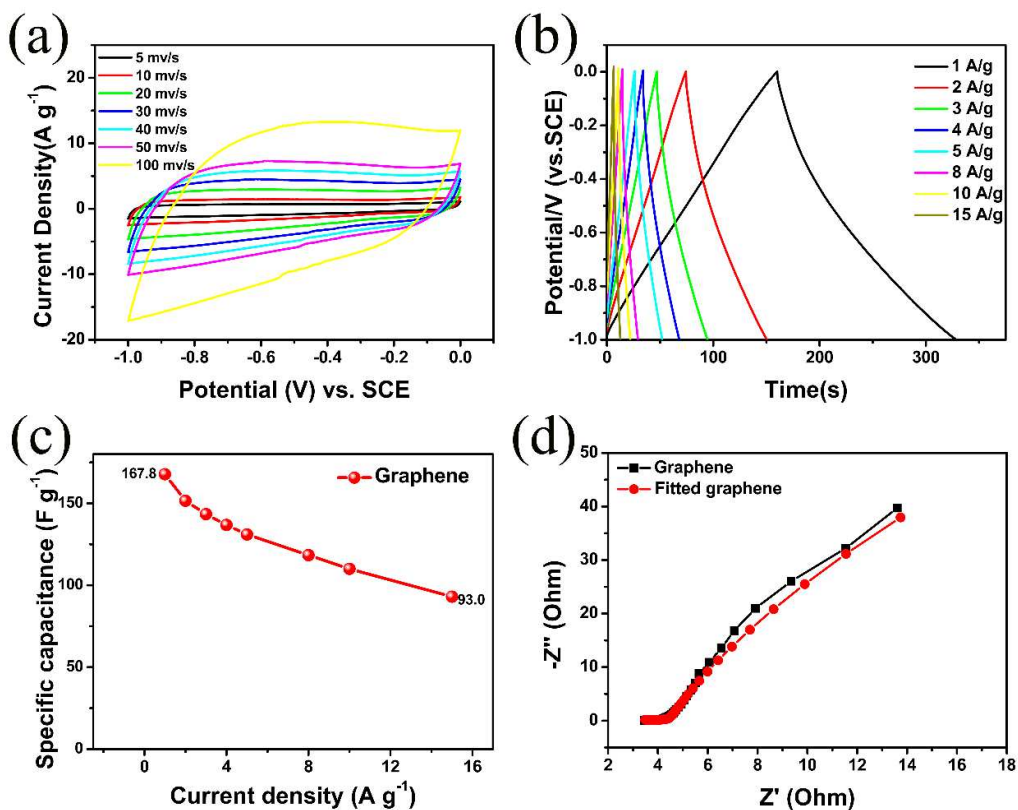
45

Fig. 9 (a) CV curves of the graphene-based electrode at different scan rates. (b) Galvanostatic charge-discharge curves of the graphene-based electrode. (c) Comparison of the specific capacitances of the graphene-based electrode at different current densities. (d) EIS spectrum of graphene-base electrode before the cycling tests.
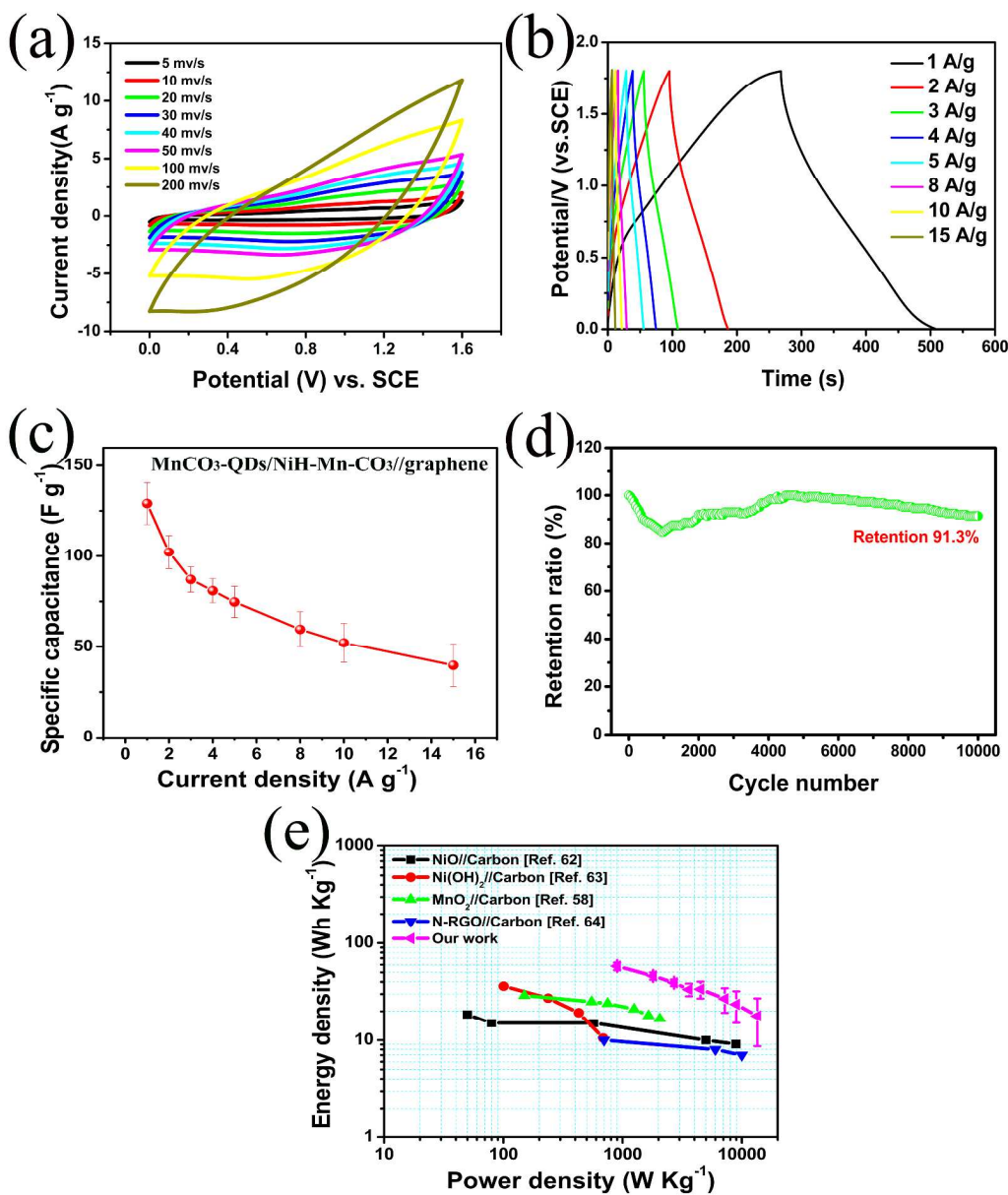
Fig. 10 (a) CV curves of the MnCO$_3$ QDs/NiH-Mn-CO$_3$//G asymmetric supercapacitor at different scan rates. (b) Galvanostatic charge-discharge curves of the MnCO$_3$ QDs/NiH-Mn-CO$_3$//G asymmetric supercapacitor. (c) Comparison of the specific capacitances of the MnCO$_3$ QDs/NiH-Mn-CO$_3$//G asymmetric supercapacitor at different current densities. (d) Cycling performance of MnCO$_3$ QDs/NiH-Mn-CO$_3$//G asymmetric supercapacitor at a current density of 5 A g^{-1}. (e) Ragone plots of the MnCO$_3$ QDs/NiH-Mn-CO$_3$//G asymmetric supercapacitor compared to the reference.

Table 1. Specific surface area, pore volume and pore size of the $Ni(HCO_3)_2$ and NiH-Mn-CO$_3$ composite materials.

Sample	Pore size (nm)	S_{BET} (m^2 g^{-1})	V_{pores} (cm^3 g^{-1})
$Ni(HCO_3)_2$	10.6	33.0	0.19
$MnCO_3$ QDs/NiH-Mn-CO$_3$ composites	2.4	117.8	0.45